

Water in protoplanetary disks with JWST-MIRI: spectral excitation atlas, diagnostic diagrams for temperature and column density, and detection of disk-rotation line broadening

ANDREA BANZATTI,¹ COLETTE SALYK,² KLAUS M. PONTOPPIDAN,³ JOHN CARR,⁴ KE ZHANG,⁵ NICOLE ARULANANTHAM,⁶
L. ILSEDORE CLEEVEs,⁷ SEBASTIAAN KRIJT,⁸ JOAN NAJITA,⁹ KARIN I. ÖBERG,¹⁰ ILARIA PASCUCCHI,¹¹
GEOFFREY A. BLAKE,¹² CARLOS E. MUÑOZ-ROMERO,¹⁰ EDWIN A. BERGIN,¹³ LUCAS A. CIEZA,¹⁴ PAOLA PINILLA,¹⁵
FENG LONG,^{11,*} PATRICK MALLANEY,¹ CHENGYAN XIE,¹¹ AND THE JDISCS COLLABORATION

¹Department of Physics, Texas State University, 749 N Comanche Street, San Marcos, TX 78666, USA

²Department of Physics and Astronomy, Vassar College, 124 Raymond Avenue, Poughkeepsie, NY 12604, USA

³Jet Propulsion Laboratory, California Institute of Technology, 4800 Oak Grove Drive, Pasadena, CA 91109, USA

⁴Department of Astronomy, University of Maryland, College Park, MD 20742, USA

⁵Department of Astronomy, University of Wisconsin-Madison, Madison, WI 53706, USA

⁶Space Telescope Science Institute 3700 San Martin Drive Baltimore, MD 21218, USA

⁷Astronomy Department, University of Virginia, Charlottesville, VA 22904, USA

⁸School of Physics and Astronomy, University of Exeter, Stocker Road, Exeter EX4 4QL, UK

⁹NSF's NOIRLab, 950 N. Cherry Avenue, Tucson, AZ 85719, USA

¹⁰Center for Astrophysics, Harvard & Smithsonian, 60 Garden St., Cambridge, MA 02138, USA

¹¹Department of Planetary Sciences, University of Arizona, 1629 East University Boulevard, Tucson, AZ 85721, USA

¹²Division of Geological & Planetary Sciences, MC 150-21, California Institute of Technology, Pasadena, CA 91125, USA

¹³Department of Astronomy, University of Michigan, 1085 S. University Ave, Ann Arbor, MI 48109

¹⁴Núcleo de Astronomía, Facultad de Ingeniería y Ciencias, Universidad Diego Portales, Av Ejército 441, Santiago, Chile

¹⁵Mullard Space Science Laboratory, University College London, Holmbury St Mary, Dorking, Surrey RH5 6NT, UK.

ABSTRACT

This work aims at providing fundamental general tools for the analysis of water spectra as observed in protoplanetary disks with JWST-MIRI. We analyze 25 high-quality spectra from the JDISC Survey reduced with asteroid calibrators as presented in Pontoppidan et al. (2024). First, we present a spectral atlas to illustrate the clustering of water transitions from different upper level energies (E_u) and identify single (un-blended) lines that provide the most reliable measurements. With the atlas, we demonstrate two important excitation effects: one related to the opacity saturation of ortho-para line pairs that overlap, and the other to the sub-thermal excitation of $v = 1 - 1$ lines scattered across the $v = 0 - 0$ rotational band. Second, from this larger line selection we define a list of fundamental lines spanning E_u from 1500 to 6000 K to develop simple line-ratio diagrams as diagnostics of temperature components and column density. Third, we report the detection of disk-rotation Doppler broadening of molecular lines, which demonstrates the radial distribution of water emission at different E_u and confirms from gas kinematics a radially-extended ≈ 170 – 220 K reservoir, close to the ice sublimation front. We also report the detection of narrow blue-shifted absorption from an inner disk wind in ro-vibrational H₂O and CO lines, which may be observed in disks at inclinations > 50 deg. We summarize these findings and tools into a general recipe that should be beneficial to community efforts to study water in planet-forming regions.

1. INTRODUCTION

The infrared spectrum of water vapor has attracted increasing interest in the community since the discovery of its forest of lines in protoplanetary disks with the

Spitzer-IRS (Houck et al. 2004) and ground-based spectrographs almost two decades ago (Carr & Najita 2008; Salyk et al. 2008). With > 1000 transitions significantly contributing to spectra at 10–37 μm , but only ≈ 150 blended features of multiple transitions that could be distinctly observed with IRS (e.g. Pontoppidan et al. 2010b), water spectra are at the same time fascinating and challenging. Most of the attraction comes from the fact that they trace inner disks at radii where rocky

Corresponding author: Andrea Banzatti
banzatti@txstate.edu

* NASA Hubble Fellowship Program Sagan Fellow

and super-Earth planet formation is expected to happen (e.g. Bitsch et al. 2019; Lambrechts et al. 2019; Izidoro et al. 2021), as shown by water line profiles when observed at high resolving power from the ground (Pontoppidan et al. 2010a; Najita et al. 2018; Salyk et al. 2019; Banzatti et al. 2023a). Water is expected to trace and significantly contribute to a number of processes that are fundamental in star formation all the way to late phases of disk evolution and planet formation (e.g. van Dishoeck et al. 2014), from the dynamics and accretion of solids (e.g. Ciesla & Cuzzi 2006a; Ros & Johansen 2013) to the development of habitable conditions (e.g. Krijt et al. 2022). Determining the water abundance in disks as a function of orbital distance and time is still one of the major goals for understanding these fundamental processes (e.g. Meijerink et al. 2009; Pontoppidan et al. 2014).

On the other hand, challenges come from the wide range of excitation conditions that water spectra trace in inner disks, including radial and vertical temperature and density gradients and non-local thermodynamic equilibrium (LTE) excitation (e.g. Glassgold et al. 2009; Najita et al. 2011; Meijerink et al. 2009; Bosman et al. 2022; Banzatti et al. 2023a). The key to distinguishing different processes and correctly interpreting the observed spectra to obtain a global view of water properties as a function of disk radius lies largely in the possibility to measure the flux and kinematics of transitions from a large range of Einstein- A coefficients (A_{ul}) and a large range in upper level energy (E_u). With Spitzer-IRS spectra, the most critical limitation to the analysis of water emission properties has come from the low resolving power ($R \sim 600\text{--}700$, or 450 km/s), blending multiple transitions and leaving fundamental degeneracies between temperature and column density in slab model fits (Meijerink et al. 2009; Carr & Najita 2011; Salyk et al. 2011). Despite the identification of some important trends with stellar temperature (Pontoppidan et al. 2010b; Pascucci et al. 2013), with stellar and accretion luminosity (Salyk et al. 2011; Banzatti et al. 2017, 2020), with the formation of an inner disk dust cavity (Salyk et al. 2011; Banzatti et al. 2017, 2020), and with the dust disk mass or radius as observed at millimeter wavelengths (Najita et al. 2013; Banzatti et al. 2020), the need for higher-resolution spectroscopy has clearly emerged as a priority for making progress in the field after Spitzer.

In spite of the paucity of high-resolution spectra due to the difficulty of observations through the Earth’s atmosphere, recent work using spectrally-resolved data from ground-based spectrographs has made some progress after the Spitzer surveys. Infrared water spectra have

been found to trace a temperature gradient in the inner regions of protoplanetary disks, when velocity-resolved line widths from a large range in energy levels have been obtained by combining data from different instruments (Banzatti et al. 2023a). A gradient is naturally expected by disk models (e.g. Glassgold et al. 2009; Meijerink et al. 2009) but evidence from the data has been slow to emerge. Early fits to Spitzer-IRS spectra initially assumed a single temperature that could well reproduce at least part of the data (Carr & Najita 2011; Salyk et al. 2011), while pointing out that the emission at longer wavelengths seemed to come from colder emission (Salyk et al. 2011; Banzatti et al. 2012). Later, some works explored using temperature gradients that could better reproduce a broader spectral range, in some cases including also far-infrared spectra (Zhang et al. 2013; Blevins et al. 2016; Liu et al. 2019). This is an aspect where the spectrally sharper view provided by JWST-MIRI can now advance the community understanding of water in inner disks (van Dishoeck et al. 2023; Kamp et al. 2023; Henning et al. 2024). Since the first MIRI observations, water emission from multiple temperatures has been confirmed by single-temperature fits to different parts of the emission (Banzatti et al. 2023b; Gasman et al. 2023; Schwarz et al. 2024) as well as two- or three-temperature simultaneous fits (Pontoppidan et al. 2024; Temmink et al. 2024) and radial gradient fits to a large part of the rotational spectrum at MIRI wavelengths (Muñoz-Romero et al. 2024a).

The identification of multiple temperature regions and characterization of their properties is a significant step towards the goal of determining the water abundance as a function of orbital distance and time. However, the detailed analysis and interpretation of water spectra remains a challenge after two years of JWST observations. Slab model fits to the observed spectra across MIRI wavelengths give different temperature and column density estimates even when similarly simple slab model tools are used (e.g. Banzatti et al. 2023b; Gasman et al. 2023; Pontoppidan et al. 2024; Schwarz et al. 2024; Temmink et al. 2024, and Salyk et al. in prep.), and it is currently unclear how much of that depends on the spectral ranges and specific lines being included (or excluded) from the fits rather than from species contamination, spectra quality (including residual fringes), and non-LTE excitation effects that have long been known (Meijerink et al. 2009) but have not been accounted for in fitting MIRI water spectra yet.

At the increased resolving power of MIRI, line blending is still an issue for carefully measuring the emission from different energy levels, due to the overlap of multiple water transitions as well as the contamination from

a number of atomic and molecular species. A common approach to correctly analyze water spectra and compare results from different studies has not yet emerged, and the identification of reliable lines for breaking degeneracies and isolating or controlling different effects (temperature from opacity gradients, LTE from non-LTE excitation) is still a priority.

It is desirable as a community to agree on a reliable line list and some simple diagnostics that will provide comparisons across samples without biases from different implementations of slab modeling tools and their (often untested) dependence on fitting different line ranges that do not properly account for contamination or non-LTE effects. As an attempt towards defining a common ground for community comparisons, in this work we provide a curated list of reliable single (un-blended) lines and demonstrate their use to describe the excitation and kinematic properties of water spectra as observed with MIRI, to provide the community with useful tools for their analysis and interpretation in the growing number of disks being collected in current and future observing cycles. In particular, we develop a general definition of water temperature and column density diagnostic diagrams that will enable empirical, line-flux-ratio comparisons across samples and datasets, to support a broad understanding of water in different conditions and its study across multiple processes that shape inner disk evolution and planet formation.

This paper is organized as follows. In Section 3 we present a spectral atlas of water emission as a general reference to support line identification and analysis, with specific focus on aspects of line blending, contamination, opacity overlap, and non-LTE excitation that are important for a correct analysis of observed spectra. With the atlas, we demonstrate a curated list of single, un-blended lines that provides the most reliable flux and broadening measurements to support global analyses of water in inner disks. Using this line list, in Section 4 we define four line ratios that provide a simple general definition of diagnostic diagrams for the temperatures and column density of water emission in individual sources as well as large samples. In Section 5 we present for the first time evidence for Doppler broadening of water lines in MIRI-MRS spectra, as well as the detection of unresolved wind blue-shifted absorption on top of disk-rotation broadened emission in a disk observed at high inclination. In Section 6 we will use this information to perform a simple Doppler mapping of water lines, which can provide an independent estimate of the emitting radii of lines from different upper level energies. We conclude in Section 7 by combining all these findings and

tools into a general recipe to support the analysis of water MIRI-MRS spectra in future samples.

2. SAMPLE & DATA REDUCTION

The data analyzed in this work were taken with the James Webb Space Telescope (JWST, Gardner et al. 2023) between February 2023 and March 2024. The disks were observed over the full wavelength coverage of 4.9–28 μm with the Medium Resolution Spectrometer (MRS, Wells et al. 2015; Argyriou et al. 2023) mode on the Mid-Infrared Instrument (MIRI, Rieke et al. 2015; Wright et al. 2023). The sample included in this work comes from three GO programs in Cycle 1 that defined the JWST Disk Infrared Spectral Chemistry Survey (JDISCS, Pontoppidan et al. 2024, Arulanantham et al. (in prep.)): 14 disks from GO-1584 (PI: C. Salyk; co-PI: K. Pontoppidan), 8 disks from GO-1640 (PI: A. Banzatti), and 3 disks from GO-1549 (PI: K. Pontoppidan) for a total of 25 disks. Sample properties are reported in Appendix A. The full sample is described in the overview paper by Arulanantham et al. (in prep.); in this paper we focus on disk spectra of T Tauri stars, i.e. we exclude 3 disks around intermediate-mass stars (HD 163296, HD 142666, and HD 143006), and we also exclude one disk in a binary system (AS 205 S) that has strong fringe residuals and binary contamination at the long MIRI wavelengths. Some spectra have been analyzed and presented before in papers from the JDISCS collaboration: CI Tau, GK Tau, IQ Tau, and HP Tau in Banzatti et al. (2023b), Sz 114 in Xie et al. (2023), FZ Tau in Pontoppidan et al. (2024), AS 209 and GQ Lup in Muñoz-Romero et al. (2024b,a), DoAr33 in Colmenares et al. 2024 (submitted).

All spectra were extracted and wavelength-calibrated with the JDISCS pipeline as described in Pontoppidan et al. (2024), which adopts the standard MRS pipeline (Bushouse et al. 2024) up to stage 2b and then uses observed asteroid spectra as calibrators to provide high-quality fringe removal and characterization of the spectral response function to maximize S/N in channels 2–4 (while a standard star is used in channel 1). Target acquisition with the MIRI imager was adopted to place all targets and asteroids on exactly the same spot on the detector with sub-spaxel precision, to ensure similar fringes and maximize the quality of their removal. For the data included in this work, we used the latest available JDISCS reduction (version 8.2) that uses the MRS pipeline version 11.17.19 and Calibration Reference Data System context `jwst_1253.pmap`. Before the gas emission analysis presented in this work, all spectra were also continuum-subtracted using a median smoothing and a 2nd-order Savitzky-Golay filter with the proce-

dure presented in Pontoppidan et al. (2024) updated to apply a final offset based on line-free regions as demonstrated in Appendix B. All the continuum-subtracted spectra are included in Appendix H.

3. A SPECTRAL ATLAS OF WATER EMISSION

Figures 1 to 4 present an atlas of water emission as observed across MIRI spectra, using as an example the spectrum of CI Tau from Banzatti et al. (2023b). This spectrum is chosen for multiple reasons: its high S/N (≈ 450 around $17 \mu\text{m}$), the detection of all molecules commonly found in disks (CO, H₂O, OH, HCN, C₂H₂, CO₂, H₂), and the detection of a large number of atomic lines (dominated by HI with 30 lines), which provide a useful template to illustrate contamination to water lines from other species. Moreover, CI Tau has been used in previous work as a base reference to identify the presence of cooler water at larger disk radii from excess emission in low-energy lines, for being a spectrum that can be described almost entirely by a single hot component (Banzatti et al. 2023b; Muñoz-Romero et al. 2024a). This property also makes it a good example to isolate other excitation effects related to line opacity and non-LTE excitation, which will be demonstrated below in this section.

The atlas is made using the functionalities of iSLAT (Jellison et al. 2024; Johnson et al. 2024) to make and export simulated spectra for single-temperature slabs of gas in LTE (defined by an excitation temperature T in K, column density N in cm^{-2} and a slab emitting area $A_{slab} = \pi R_{slab}^2$ in au^2 , e.g. Carr & Najita 2011; Salyk et al. 2011; Banzatti et al. 2012) for multiple molecules and visualize the individual transitions blended at the resolving power of MIRI, using line properties from HITRAN (Gordon et al. 2022). Each figure shows model spectra for emission at different temperatures: a “hot” water component (850 K) and a “warm” water component (400 K) as representative of typical temperatures found from slab fits to a total sample of ten disks in previous work (Banzatti et al. 2023b; Muñoz-Romero et al. 2024a; Temmink et al. 2024). While these temperature components have been found to describe well the rotational water emission across MIRI wavelengths (12–27 μm), with hotter emission generally dominating shorter wavelengths, an additional “cold” 170–190 K component, where detected, becomes prominent at longer MIRI wavelengths, in particular in two lines near 23.85 μm with upper level energy ≈ 1500 K (Zhang et al. 2013; Banzatti et al. 2023b; Muñoz-Romero et al. 2024a; Temmink et al. 2024). This component is of particular interest because it traces a temperature consistent with the ice sublimation/condensation front (the

“snowline”) in inner disks (e.g. Pollack et al. 1994; Saselov & Lecar 2000; Lodders 2003). The very different spectral line flux distribution of these three components across infrared wavelengths provides a useful general tool for their identification in MIRI spectra, as will be demonstrated below in Section 4.

Other molecules are plotted in different colors to illustrate where water emission is contaminated by other species, including atomic (which are marked with dotted lines and labelled for identification). The adopted slab model parameters for each molecular model are reported in Appendix G; these are just representative models, not fits to the data, and include two components of OH to approximately reproduce its complex non-LTE emission, but not its visible asymmetry from prompt emission (for detailed analyses on OH excitation in disks, see e.g. Carr & Najita 2014; Tabone et al. 2021, 2024; Zannese et al. 2024).

3.1. Using the atlas

Figures 1 to 4 provide a general reference for several aspects that are helpful for the analysis of water spectra as observed with MIRI-MRS, which will be elaborated on below:

1. the level of blending and confusion between different energy levels in each observed water line;
2. water lines that are single, i.e. not blended with other water transitions from different levels at the temperature considered here;
3. the relative emission in higher- versus lower- E_u across MIRI wavelengths, which is connected to the emission from different temperatures;
4. contamination of water emission from other molecules and atoms;
5. saturation from line opacity overlap and non-LTE excitation of higher vibrational levels ($v > 0$).

3.1.1. Water transitions from different E_u

The first three points in the list can be visualized as follows. Under the water models in Figures 1 to 4, the individual transitions that make the observed blended emission are plotted with vertical dashed lines, color-coded with a gradient from magenta (higher- E_u) to cyan (lower- E_u) to reflect the upper level energy. As in iSLAT, the height of these lines in the plot is proportional to their intensity, to visualize their relative contribution in each blend. To provide a maximum case of line blending, we visualize lines from the 850 K model; at lower temperatures, the higher-energy transitions are less excited and therefore more lines may be dominated by a

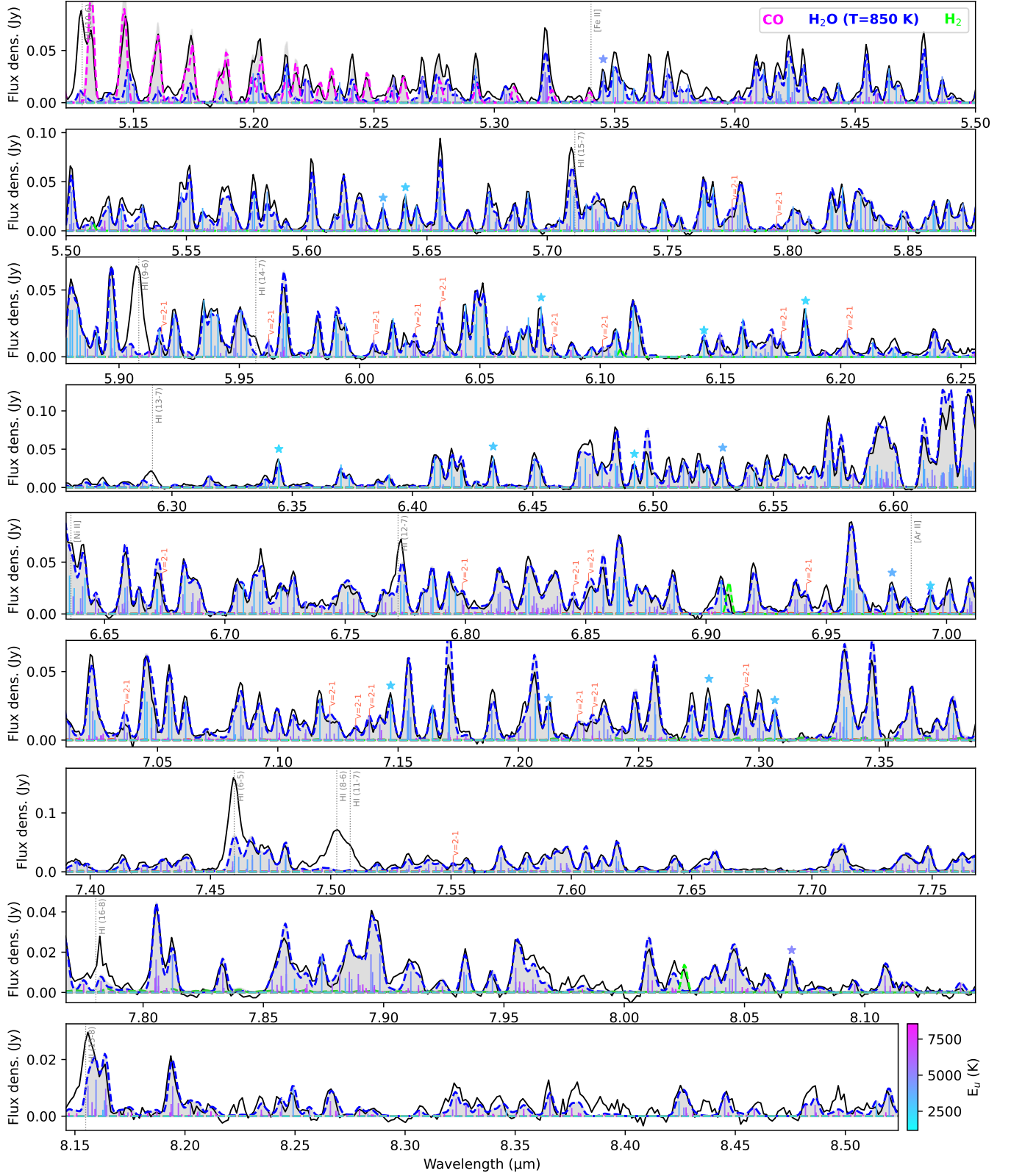


Figure 1. Atlas of water emission in MIRI-MRS spectra (see Section 3), using CI Tau as an example (shown in black). Vertical lines mark transition wavelengths, color-coded according to the upper level energy E_u as shown in the color bar. Lines marked with a star (color-coded in the same way) are from the list of single (un-blended) lines used in this work (Appendix E). Slab models (top-right inset, Appendix G) are added with dashed lines on top of the data. The ro-vibrational band at 5–8 μm is dominated by $v = 1 - 0$ lines (all lines unless labelled), but there are some prominent $v = 2 - 1$ lines that are detected (see Section 3). *Figures 1 to 4 will be made interactive in the online journal published version, to access individual line properties.*

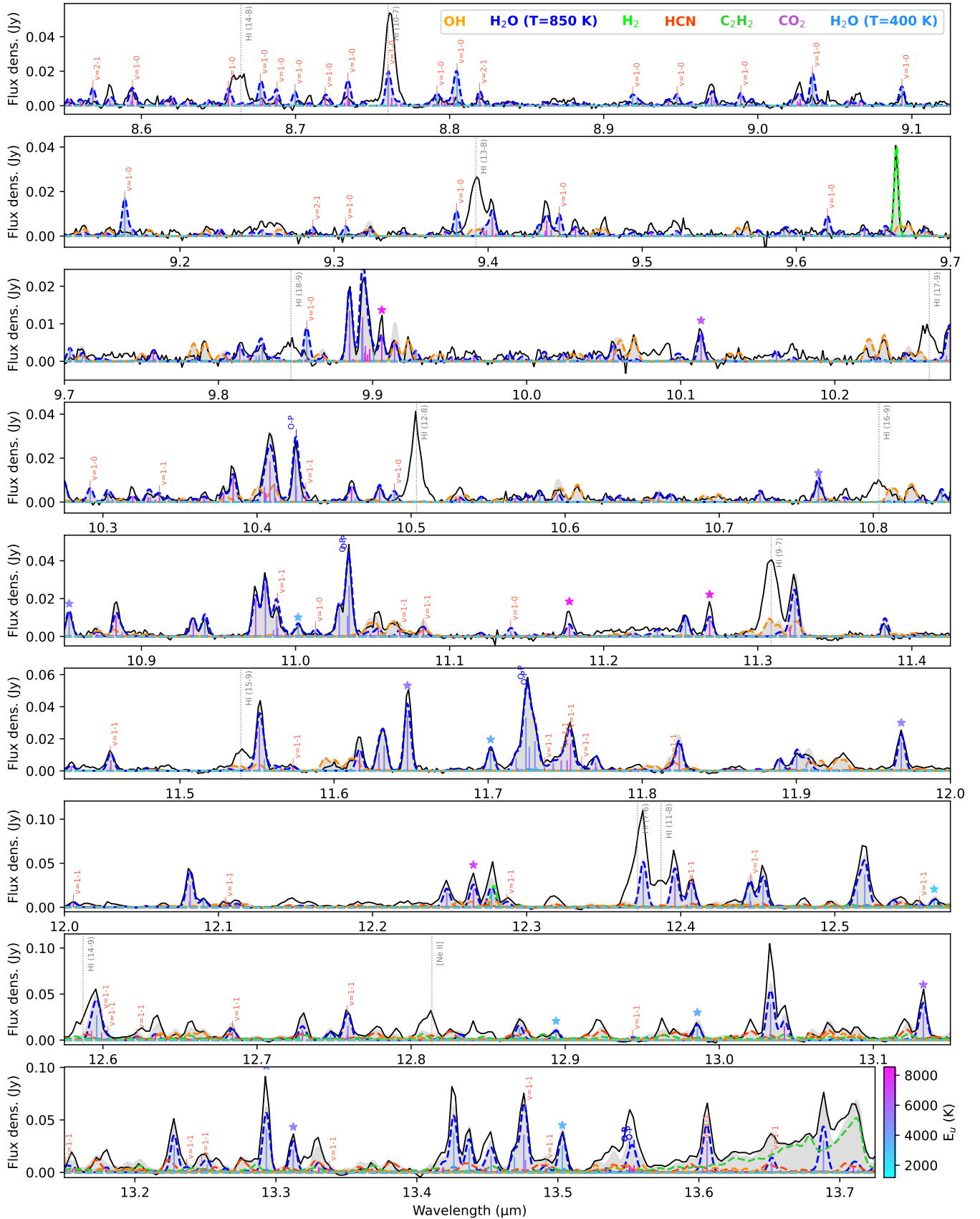


Figure 2. Atlas of water emission in MIRI-MRS spectra (continued from Figure 1): the rotational spectrum at intermediate wavelengths. The emission is dominated by $v = 0 - 0$ lines (all lines unless labelled), but there are lines from the first vibrational state including several prominent $v = 1 - 1$ lines (Section 3.1.4). Ortho-para line pairs are labelled “O-P” (see Section 3.1.3).

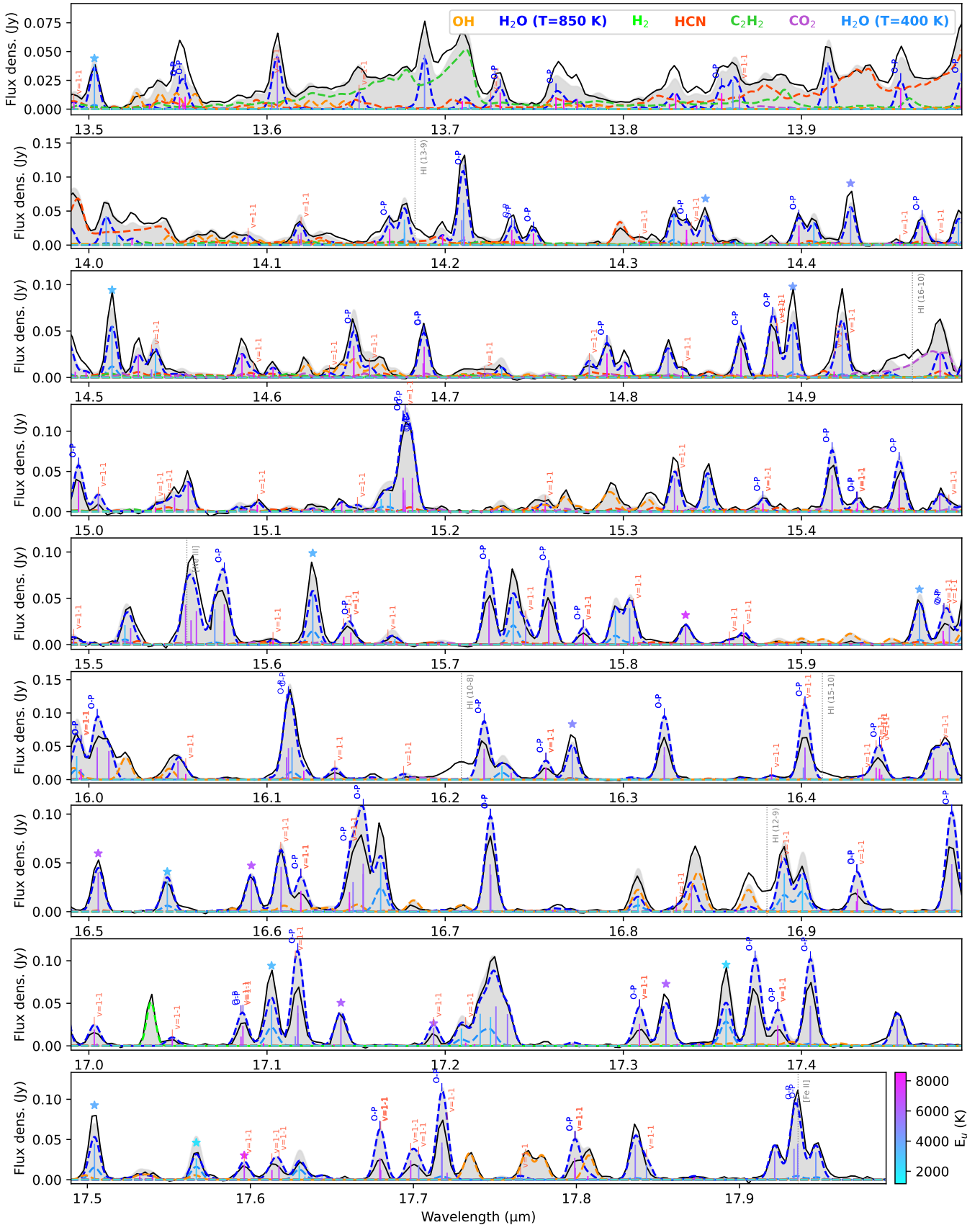


Figure 3. Atlas of water emission in MIRI-MRS spectra (continued from Figure 2): the rotational spectrum at intermediate wavelengths. The emission is dominated by $v = 0 - 0$ lines (unlabelled), but there are several prominent $v = 1 - 1$ lines (Section 3.1.4). Ortho-para line pairs are labelled “O-P” (see Section 3.1.3).

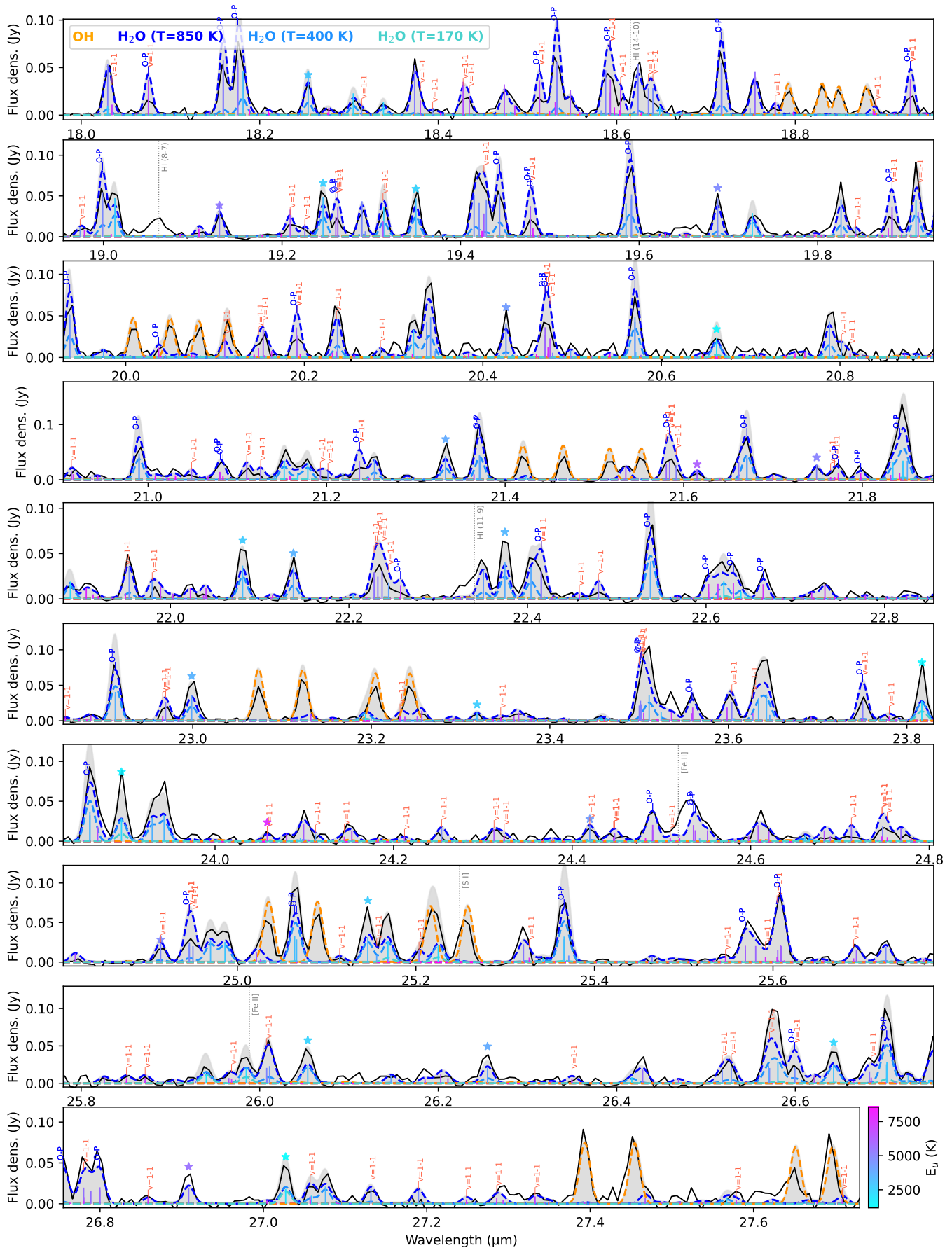


Figure 4. Atlas of water emission in MIRI-MRS spectra (continued from Figure 3): the long MIRI wavelengths. A colder component of water emission (~ 170 K) is most prominent in two low-energy ($E_u \sim 1500$ K) lines near $23.85 \mu\text{m}$ (Section 4).

single, lower-energy transition. However, in this sample we find that disk spectra generally have the high-energy lines significantly excited except for a few exceptions (see Appendix H and Salyk et al. in prep.), therefore the spectral atlas figures presented here should provide a useful general guidance.

From these figures, it is possible to obtain a quick idea of how many transitions contribute significantly to each observed line/blend, and whether higher- rather than lower-energy transitions are blended in a given observed line. In cases where line clustering is too dense and/or the coloring system is not sufficient to identify individual lines in Figures 1 to 4, we recommend using iSLAT¹ to inspect interactively any line blends of choice for different temperature and column density values. With this procedure, we have identified a list of single (unblended) water lines whose properties reflect the emission from individual upper levels (Section 3.2); this list provides reliable measurements for a number of analysis goals, which will be demonstrated below.

3.1.2. Contamination from different species

For the fourth point, the atlas provides quick identification of contamination from other molecules and atoms. For lines with lower contrast in the figure, we suggest the use of iSLAT for interactive visualization and inspection. Depending on their relative strength, most water lines between 12 and 16 μm are typically contaminated by lines from OH, HCN, C_2H_2 , and CO_2 . For this reason, in this work we only use a few lines for analysis in this region, lines that in conditions found to be typical in this sample are still dominated by water emission (Figures 2 and 3). Atomic lines, in particular from HI, are scattered across MIRI wavelengths and also need to be carefully checked to avoid contamination.

Vice versa, the atlas can be used to identify atomic emission lines that are the least contaminated by water or other molecules. In the case of HI, the most clean, strong lines are (upper-lower levels): 12-8 (10.50 μm), 10-8 (16.21 μm), 8-7 (19.06 μm), 10-7 (8.76 μm), 14-8 (8.66 μm), 9-6 (5.91 μm). These lines can generally be measured from MIRI spectra even when water emission is present; other lines require subtracting a water model first. Other atomic species of common interest, including [NeII] and [NeIII], are all contaminated by water or other molecules and should generally be measured in water-subtracted spectra, unless water emission is absent or very weak. Examples of the water-subtraction process using Spitzer spectra can be found in Salyk et al.

(2011); Rigliaco et al. (2015), and with MIRI spectra in Grant et al. (2023).

3.1.3. Mutual line opacity saturation

For the fifth point in the list above, the atlas identifies transitions that are of special interest for understanding the excitation and observed flux of specific water lines. Previous work showed that parts of the infrared organic emission features at 13–14 μm may become highly optically thick and saturate due to the dense line clustering. This was observed in extreme high-column density conditions by Tabone et al. (2023) in the emission feature of C_2H_2 as observed with MIRI in the protoplanetary disk of a low-mass star. It has not been demonstrated yet where this effect may matter for infrared water spectra, instead, in spite of the fact that line opacity overlap has previously been included in modeling Spitzer spectra (Carr & Najita 2011; Salyk et al. 2011). With the increased resolving power of MIRI-MRS, we can now better observe where line opacity overlap matters the most. In the case of water, the mutual opacity saturation becomes relevant in several ortho-para (O-P) line pairs that share the same E_u but have different statistical weight and overlap exactly or very closely in wavelength; in these cases, each line contributes to the opacity of the other line and the observed blended line saturates at lower values of the column density. This effect can be easily identified with iSLAT, which over-predicts the flux of all these line pairs by ignoring this mutual saturation effect.

To demonstrate the opacity saturation effect in the case of water lines, we add in Figure 5 a new model that uses the same parameters as the iSLAT hot water model, but made with a code that includes mutual line opacity saturation (`spectools-ir`, Salyk 2022). The simulated spectra from the two codes perfectly match as they should (since they are equivalent, otherwise) except for the ortho-para line pairs, where `spectools-ir` provides a very good match to the data in contrast to the iSLAT model. Therefore, line overlap should be accounted for when fitting water spectra, because many O-P lines pairs are close or coincident in wavelength, such that their fluxes do not simply add when the lines optical depth increases towards thick conditions. For details on existing code that implements this effect for water emission, see `spectools-ir`² (Salyk 2022) and `iris`³ (Munoz-Romero et al. 2023).

3.1.4. Non-LTE excitation of lines in $v = 2$ and $v = 1$

¹ Available at <https://github.com/spexod/iSLAT>.

² Available at https://github.com/csalyk/spectools_ir.

³ Available at <https://github.com/munozcar/IRIS>.

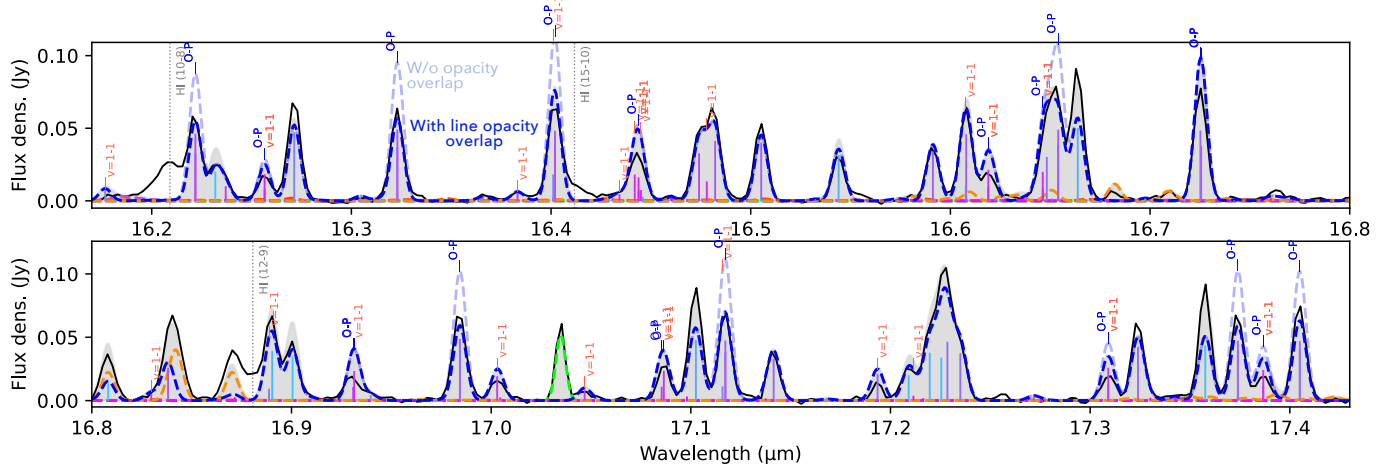


Figure 5. Portion of Figure 3 illustrating the effect of mutual line opacity saturation. The iSLAT hot water model from Figure 3 is now shown in light blue, and a new model with the same parameters but including line opacity overlap is shown in bold blue (using `spectools.ir`, Salyk 2022). Accounting for line saturation correctly reproduces the reduced emission from the ortho-para line pairs, but the $v = 1 - 1$ lines are still over-predicted because both models assume LTE (compare to Figure 6).

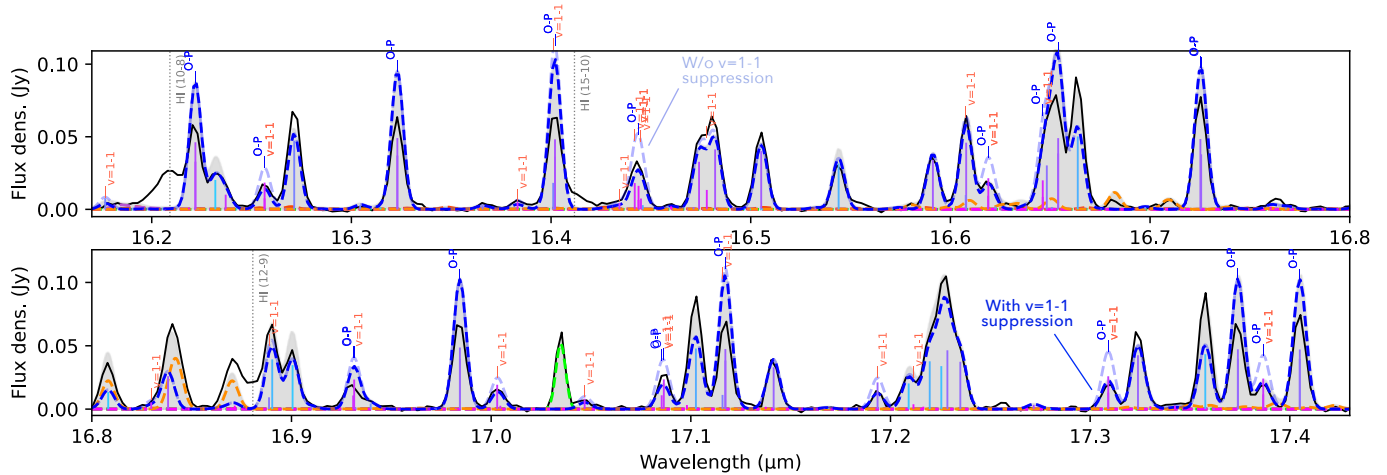


Figure 6. Same as Figure 5, but here illustrating the effect of non-LTE excitation. The iSLAT model is shown in light blue, and the same model with the $v = 1 - 1$ lines divided by a factor of 2 is shown in bold blue.

Another important effect included in the fifth point in the list above is related to non-LTE excitation. Non-LTE excitation of infrared water emission has been discussed in detail in previous work (Meijerink et al. 2009), and recently proposed to explain the observed suppression of the ro-vibrational bands in comparison to the excitation of pure rotational lines (see Bosman et al. 2022; Banzatti et al. 2023a). The origin of this effect comes from the very different critical densities of water lines from different bands, of the order of 10^{13} cm^{-3} for the ro-vibrational lines in comparison to $10^8 - 10^{11} \text{ cm}^{-3}$ for the rotational lines (see summary in Figure 13 in Banzatti et al. 2023a). This difference implies that rotational lines thermalize at lower gas densities, while ro-vibrational lines may be sub-thermally excited if the

gas density of the emitting layers in inner disk does not reach $\sim 10^{13} \text{ cm}^{-3}$.

To simulate the sub-thermal excitation of ro-vibrational lines, in Figure 1 we used a factor 4 decrease in emission in comparison to the model of the rotational lines at longer wavelengths (see model parameters in Appendix G), which is enough to approximately reproduce the ro-vibrational band in CI Tau. A similar factor was found to approximately reproduce the ro-vibrational band also in the case of FZ Tau in Pontoppidan et al. (2024). Even with this global reduction factor, $v = 2 - 1$ lines are generally over-predicted in comparison to the $v = 1 - 0$ lines (Figure 1), pointing again to non-LTE excitation (for this effect in the case of CO lines, see e.g. Banzatti et al. 2022; Ramírez-Tannus et al. 2023). We remark that fits to higher-resolution (but

much smaller spectral range) spectra from the ground suggested slightly higher temperatures of ≈ 1000 K for the ro-vibrational water band near $5 \mu\text{m}$ (Banzatti et al. 2023a), which is dominated by higher energy levels (4500–9500 K) and therefore it is more sensitive to gas at higher temperature. However, these higher-energy lines are much weaker and generally blended at the resolution of MIRI, where strong un-blended lines are dominated by lower-energy levels (Figure 1). We also remark that the suppression factor needed by the $v = 1 - 0$ lines in comparison to the rotational lines cannot be explained simply by a smaller emitting area (Muñoz-Romero et al. 2024a), which is nonetheless demonstrated by velocity-resolved line widths from ground-based surveys (Banzatti et al. 2023a) and now also from MIRI spectra (Section 5.1).

The excitation mismatch between different vibrational levels is also very visible in the $v = 1 - 1$ lines, as resolved by MIRI-MRS and shown in this work for the first time. There is a large number of strong $v = 1 - 1$ lines intermixed to the $v = 0 - 0$ lines in the main rotational emission region at longer wavelengths ($> 10 \mu\text{m}$, Figures 3 and 4), and these are over-predicted by fits to the $v = 0 - 0$ lines as expected in case of sub-thermal excitation of higher vibrational bands (Meijerink et al. 2009). It should be noted that the $v = 1 - 1$ lines are still over-predicted by the `spectools-ir` model in Figure 5, since it still assumes LTE. This is not an issue of the single-temperature approximation: the over-prediction of $v = 1 - 1$ lines still happens even when modeling the water spectrum as the sum of two temperatures or as a temperature gradient (by inspecting figures reporting the best-fit models, the over-prediction of some of these lines can in fact be recognized in Pontoppidan et al. 2024; Muñoz-Romero et al. 2024a; Temmink et al. 2024).

As a simple test, we show in Figure 6 that these lines, similarly to the $v = 1 - 0$ band at shorter wavelengths, match the observed data reasonably well with the simple suppression of their flux by a single factor common to all lines. In the case of CI Tau, for the $v = 1 - 1$ lines this factor is ~ 2 . A detailed analysis of the relative excitation of $v = 1 - 0$ and $v = 1 - 1$ lines in the sample included in this work is deferred to future work.

3.2. List of single un-blended lines used in this work

By applying all the criteria described above in this section, we selected a list of un-blended water lines each from a single upper level that avoid contamination from other species as observed with MIRI-MRS, a list that is used for the analysis presented in this work. We remark that depending on the specific spectrum and the analysis goals and methods, other lines can certainly be

measured and used in MIRI spectra; here we aim at providing a reliable line list that can be measured directly from the spectra in the typical conditions found in this sample, without subtracting other molecular models or attempting to de-blend lines first. In comparison to the lists of single lines available in iSLAT, to provide more reliable data for line broadening measurements we have excluded lines that are significantly blended on their wings (Section 5.1). The full line list used in this work is marked with a star in Figures 1 to 4 and reported in Appendix E.

A subset of this larger line list that has a central role in our analysis is between 14.4 and $17.6 \mu\text{m}$ (Figure 3). These lines will be used for excitation and broadening diagnostics as explained in Sections 4 and 5. The advantages of using lines in this spectral range are multiple: they are in one of the highest-S/N and highest resolving power parts of the MIRI spectrum (Pontoppidan et al. 2024), they are stronger than lines at shorter wavelengths and are free from contamination from organics, and they are close to the H_2 S1 line at $17.04 \mu\text{m}$, which provides a useful anchor point for the MIRI resolving power (see below Section 5.1). In cases where organic emission is particularly strong relative to water emission, water lines in this list at 12 – $16 \mu\text{m}$ may be significantly contaminated by HCN, C_2H_2 , or CO_2 ; in this sample, this is the case for DoAr 25 (with HCN), GO Tau (with C_2H_2), and MY Lup (with CO_2).

4. DEFINITION OF WATER LINE-RATIO DIAGNOSTIC DIAGRAMS

With the list of single lines selected in Section 3, we can now proceed to an update and generalization of the distribution of water emission from different temperatures introduced in previous work. For measuring emission line properties from the spectra we use iSLAT, which implements the least-square minimization code `lmfit` (Newville et al. 2014) to perform single-Gaussian fits and measure the line centroid, full width at half maximum (FWHM), and flux and their uncertainties.

When fitting for two temperatures as well as a temperature gradient, previous work found CI Tau to be the disk most dominated by a hot water component, while GQLup to be one with strong emission from additional cooler water at larger radii (Muñoz-Romero et al. 2024a). We show these two extreme cases in Figure 7 to illustrate how the temperature distribution in a MIRI spectrum can be visible by eye from the spectral line flux distribution, i.e. the distribution of line flux as a function of wavelength. This distribution is rather flat with wavelength (i.e. the strongest lines have similar flux across MIRI wavelengths) in the case of a hot-dominated

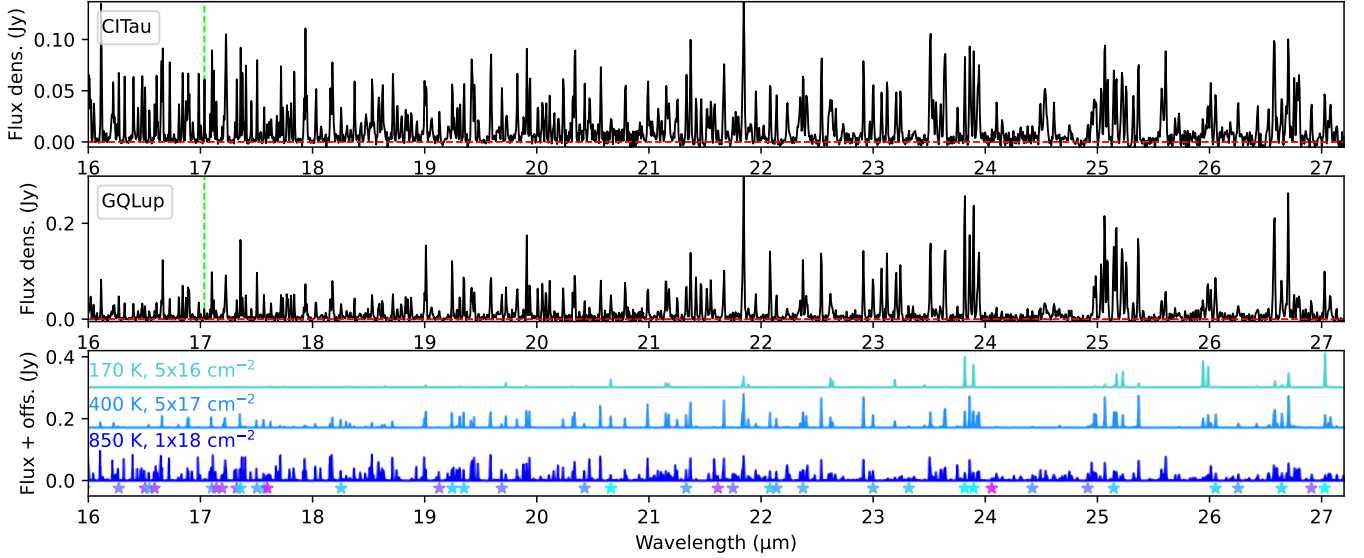


Figure 7. Representative water spectra for a hot-dominated (CI Tau) and cool-dominated (GQ Lup) disk are shown in comparison to temperature-component models (bottom). The different spectral line flux distribution is very visible, with the strongest lines having similar flux across MIRI wavelengths in the case of a hot-dominated spectrum, versus increasingly stronger lines at longer wavelengths when emission from cooler water is present. The full sample is shown in Appendix H.

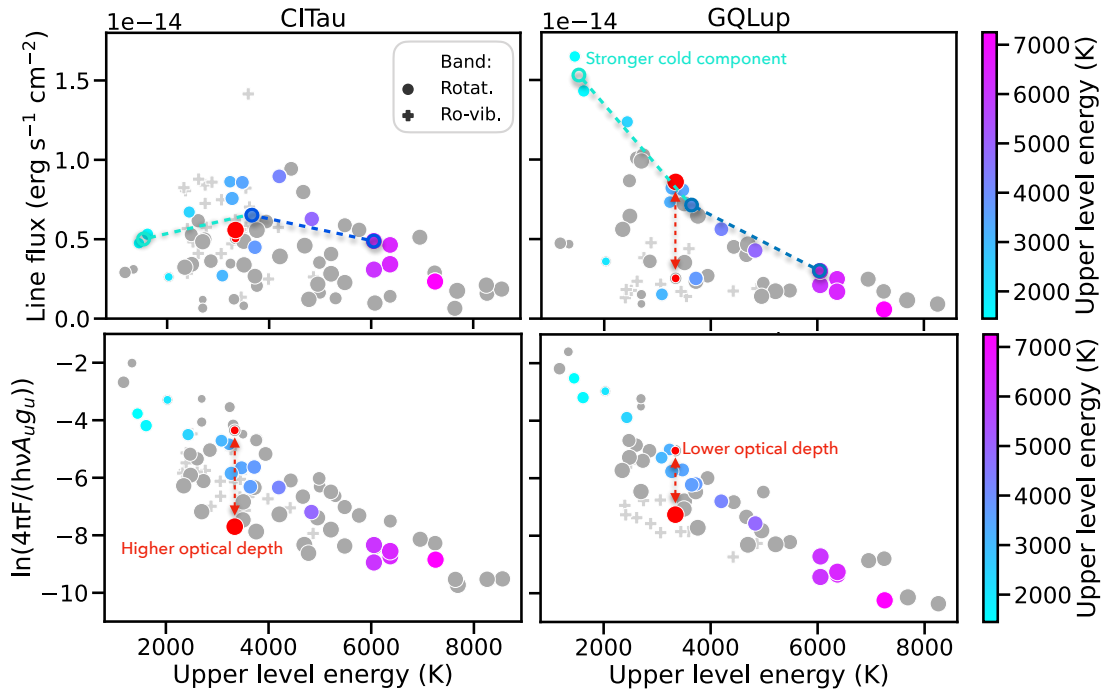


Figure 8. Demonstration of line selection for definitions of line ratios used in Figure 9, showing line fluxes (top) and the rotation diagram (bottom) as a function of the upper level energy of individual water transitions. The very different spectral line flux distribution of the hot-dominated CI Tau and cool-dominated GQ Lup shown in Figure 7, here shown as a function of E_u , is once again very visible. Grey datapoints are all lines used in this work (Appendix E), colored datapoints are the line selection from Section 3.2. The line ratios at 1500, 3600, and 6000 K reflect the relative flux in different temperature components. The line ratio at 3340 K between two lines with very different A_{ul} (shown proportional to the symbol size) reflects the optical depth. Rotation diagrams for the whole sample are shown in Appendix F.

spectrum (CI Tau), while it shows increasingly stronger lines at longer wavelengths when emission from cooler water is present (GQ Lup). This different spectral line flux distribution is exemplified at the bottom of the figure using slab models at three temperatures representing properties found in previous work as explained in Section 3 (assuming a cold component at 170 K as found from a fit to MIRI and IRS low-energy lines in Banzatti et al. 2023b), for reference.

Leveraging the different spectral line flux distribution of different temperature components, previous work defined an empirical “cool water excess” by using the hot-dominated CI Tau spectrum as a comparative template for other disks, and by measuring excess emission in the lower-energy transitions from a large number of single lines measured across MIRI wavelengths (Banzatti et al. 2023b). In this new work, we develop a simpler diagnostic that can be applied broadly to future analyses of disk samples observed with MIRI. We use: i) a hot water model as the base to define the minimum flux in low-energy lines in absence of emission from cooler water, and ii) a curated, short list of emission lines from single transitions spanning E_{up} between 1400 and 6000 K that maximize data quality in terms of S/N and resolving power, absence of residual fringes, and absence of contamination from other species in typical emission conditions as observed in this work’s sample.

4.1. Diagnostic lines for temperature and density

In Figures 8 and 9, we demonstrate the selected lines and their use as proxies for temperature distribution and column density of the water spectra. These lines are reported in Table 1. From the main list of single lines defined above in Section 3, three lines are selected to span the entire range of E_u covered by MIRI at the two extremes (near 1500 K and 6000 K, avoiding lines at higher E_u that are typically weaker and more likely affected by non-LTE excitation), and at intermediate E_u (near 3600 K). These lines provide three line ratios that capture the relative emission from different temperature components: the line flux ratio between transitions from 3600 and 6000 K (capturing the relative strength of a “warm” water component, here taken at ≈ 400 K), and the line flux ratio between transitions from 1500 and 3600 K or 6000 K (for the relative strength of a “cold” water component, here taken at ≈ 170 K).

While the low-energy lines near 23.85 μm were already identified as good tracers of sublimation temperatures (~ 170 K) water in previous work (Zhang et al. 2013; Banzatti et al. 2023b), the two lines we use here to trace water at higher temperatures are selected from the 17–17.6 μm range, which achieves the highest S/N and a

Table 1. List of transitions used for line ratios in Figure 9.

Wavelength (μm)	Transitions (upper-lower) (level format: $v_1v_2v_3 J_{K_a K_c}$)	A_{ul} (s^{-1})	E_u (K)
Label: H₂O 1500 K (temperature tracer)			
23.81676	000-000 8 ₃₆ – 7 ₀₇	0.61	1448
23.89518	000-000 8 ₄₅ – 7 ₁₆	1.04	1615
Label: H₂O 3600 K (temperature tracer)			
17.50436	000-000 13 ₄₉ – 12 ₃₁₀	4.94	3646
Label: H₂O 6000 K (temperature tracer)			
17.32395	000-000 16 ₈₉ – 15 ₇₈	41.5	6052
Label: H₂O 3340 K (density tracers)			
13.50312 (a)	000-000 11 ₇₄ – 10 ₄₇	0.49	3341
22.37473 (b)	000-000 11 ₇₄ – 10 ₆₅	25.3	3341

NOTE—For the 1500 K lines, in Figure 9 we take the combined flux of the two lines listed in this table, as explained in Section 4. Lines are identified and inspected using iSLAT (Jellison et al. 2024; Johnson et al. 2024). Line properties are from HITRAN (Gordon et al. 2022). The full line list used for other parts of the analysis in this work is reported in Appendix E.

high resolving power at MIRI wavelengths (Section 5.1). The line selection from different options with similar E_u was made such that the 850 K model adopted in this work has all line ratios with a value of ~ 1 , making it a convenient, easy reference (the 850 K model sits near 1,1 in each plot in Figure 9). For this reason, the 1500 K line flux is taken as the sum of the two transitions in Table 1.

Additionally, we identify two lines from the same upper level with $E_u = 3341$ K and statistical weight of 69 that have very different Einstein- A coefficients: 0.49 and 25.3 s^{-1} . This line pair traces the spectral line flux distribution in MIRI spectra near the peak of maximum spread in the rotation diagram (Figure 8) and it is one of the few we could find among single un-blended lines that are strong enough to be typically detected in disks, providing very useful measurements to help estimating the column density. In fact, in optically thin conditions these lines will be very different in flux, as the low- A_{ul} line will be weaker, while in optically thick conditions the two lines will have similar flux, and their flux ratio (defined as the higher A_{ul} line, labelled “b”, divided by the lower A_{ul} line, labelled “a”) will reflect these two regimes. As described in detail in Banzatti et al. (2023a), a lower column density in the rotation diagram will be observed as a lower spread in the data, while the opposite will be seen with a larger column density.

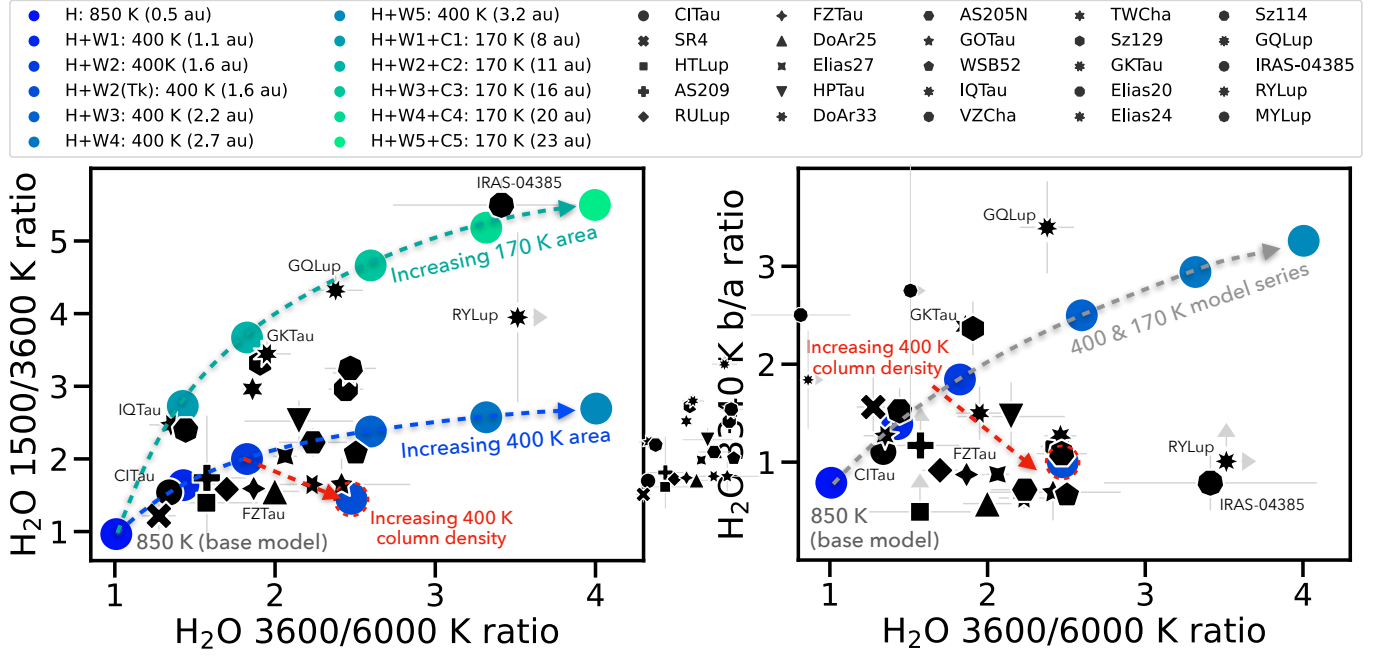


Figure 9. Definition of water diagnostic diagrams using line flux ratios as described in Section 4 and Table 1. Lower limits are marked with grey arrows. Some targets mentioned in the text are labelled for easier visualization. The red arrow marks the direction of increasing column density for the 400 K component, as shown by the model encircled in a dashed red line (model “H+W2 (Tk)” that has a 10 times higher column density than model “H+W2”). Parameters for all the models in this figure are reported in Table 9 in Appendix G. The diagram using the 1500/6000 K line ratio is included in Appendix F.

These different regimes are well illustrated by the two examples included in Figure 8.

4.2. Definition of general water diagnostic diagrams

The four line flux ratios defined above are shown in Figure 9 (and in Appendix F) as measured in the entire disk sample included in this work. The spectra of CI Tau and SR 4 lie closest to the hot model as expected, being both dominated by the hot component and having only minimal warm component (for SR 4, see Appendix H). The rest of the sample aligns with two series of models defined as follows. First, we take the base hot model and add a progressively larger amount of warm water component (400 K) by increasing its emitting area to mimic a larger warm-water-rich disk region as reported in Appendix G (where we report the corresponding gas mass in units of micro-Earth masses, which is not the total water mass but just the mass that would be observable in MIRI spectra; see e.g. Bosman et al. 2022). About 50% of the sample aligns well with this model series, consistent with hot spectra enriched with some warm (~ 400 K) water emission but no need for colder (< 200 K) water. A notable example to highlight is the case of FZ Tau, where indeed no water cooler than 300–500 K was detected (Pontoppidan et al. 2024; Muñoz-Romero et al. 2024a). Relative to CI Tau, the position of FZ Tau in Figure 9 also suggests a slightly more ex-

tended and more optically thick warm component, supporting what found from radial-gradient fits to the line fluxes (Muñoz-Romero et al. 2024a).

The rest of the sample, instead, falls above this model series requiring extra enrichment at cooler temperatures to increase the flux of the 1500 K transitions. This colder emission has been modeled in a few disks in previous work, which found temperatures of 170–190 K (Banzatti et al. 2023b; Muñoz-Romero et al. 2024a; Temmink et al. 2024). In this work, we introduce a new simple diagnostic for the coldest temperature that is detected with MIRI: the flux asymmetry between the two 1500 K transitions, where cooler temperatures produce stronger emission in the 1448 K line at $23.867\mu\text{m}$. In Figure 10, we demonstrate this new diagnostic by taking a grid of slab models between a temperature of 150 K and 850 K and a column density between 10^{16} cm^{-2} (giving optically thin emission) and 10^{19} cm^{-2} (giving optically thick emission), spanning the entire range of conditions adopted above in this work. We simulate their spectra as done for the models in Figure 4 and measure the line flux of these two lines over the same range as done for the data. We then plot the model line ratio as a function of the slab temperature for the different curves in column density in Figure 10. This model grid illustrates that temperatures above 350 K produce a stronger 1615 K line, or an equal flux in the two lines (a ratio

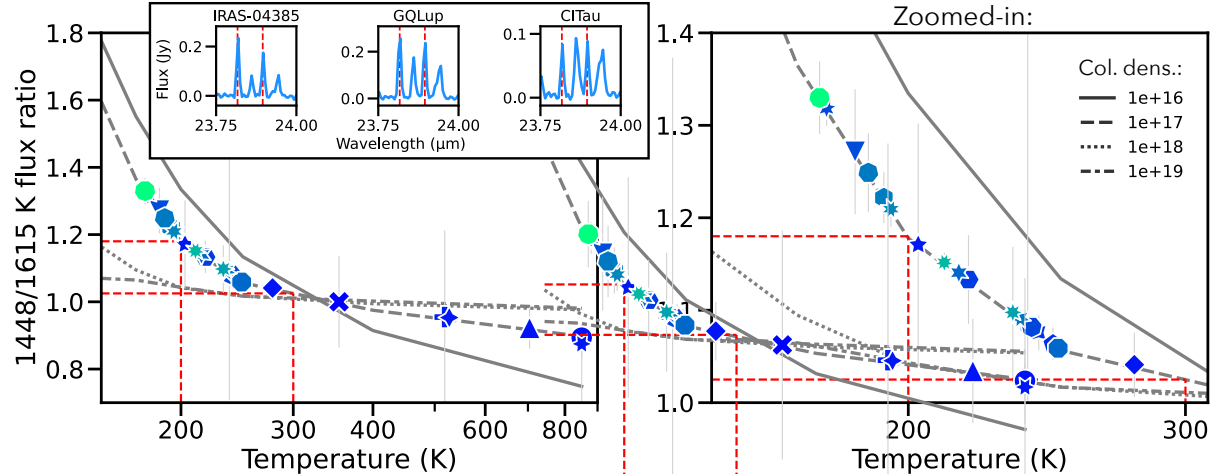


Figure 10. Diagnostic diagram for the coldest water emission detected at MIRI wavelengths, using the flux ratio between the two low-energy lines near $23.85 \mu\text{m}$ illustrated in three examples in the top-left inset (for their properties, see Table 1). Slab models in LTE are shown with grey lines over a range of column densities between 10^{16} cm^{-2} (giving optically thin emission) and 10^{19} cm^{-2} (giving optically thick emission), as show in the legend. The sample analyzed in this work is distributed along the 10^{17} cm^{-2} model according to their measured line flux ratios; target markers are the same as in Figure 9 and the color-coding follows that of the model tracks in that figure, from darker blue symbols for disks along the 400 K model track to lighter green symbols for disks along the 170 K model track.

of ~ 1) in case of higher column density. At temperatures $< 350 \text{ K}$, the 1448 K line becomes increasingly stronger, especially for lower values of column density. We distribute the line flux ratios measured in the sample along the 10^{17} cm^{-2} model, assuming it represents an average column density for this component (as found for the coldest water detected in radial temperature profiles in Muñoz-Romero et al. 2024a). With this column density, in five disks the line asymmetry gives evidence for a temperature of 170–200 K (IRAS-04385, GK Tau, IQ Tau, Sz 114, Sz 129), three more for a temperature 200–220 K (GQ Lup, RY Lup, AS 205 N) and seven more a temperature of 220–250 K (HP Tau, VZ Cha, TW Cha, Elias 24, Elias 20, WSB 52, Elias 27). In general, these models show that a line ratio > 1 requires temperatures $< 350 \text{ K}$ and a ratio > 1.2 temperatures $< 220 \text{ K}$ for any column density explored here. In total, therefore, about 50% of this sample has evidence for water emission at temperatures 170–250 K, close to and consistent with the snowline region. To confirm the exact temperature and determine the column density of water near and across the snowline, lower-energy lines at longer wavelengths need to be included as previously provided from Spitzer or Herschel (Zhang et al. 2013; Banzatti et al. 2023b) or from a future far-infrared observatory (Pontoppidan et al. 2018, 2023; Kamp et al. 2021).

To account for the colder emission, in a second series of models in Figure 9 we take the first series and progressively add a larger amount of water consistent with the snowline region (here assuming 170 K) by

increasing its emitting area to mimic a larger cold-water-rich disk region. The second model of this series (H+W2+C2) aligns well with GK Tau, which was identified to have a prominent cold water excess in comparison to CI Tau (Banzatti et al. 2023b) and where temperature gradient fits have found that water is detected down to sublimation temperatures near the snowline ($\sim 180\text{--}200 \text{ K}$, Muñoz-Romero et al. 2024a). Another disk that was found with strong emission from colder water down to ice sublimation temperatures was GQLup, as already stated above, which lies near the third model in this series (H+W3+C3), consistent with its more extended cold water component in comparison to GK Tau (Muñoz-Romero et al. 2024a). A disk with an even stronger cold water component is now found in IRAS 04385+2550, a young disk in Taurus. Cases where the hot water emission is strongly reduced or absent and the observed spectrum can be reproduced mostly by a warm and/or cold water component may provide lower limits in some line flux ratios, as is the case for RY Lup and MY Lup in this sample (the latter sits at $\approx 5,6$ in the left plot in Figure 9 and is reported in Salyk et al. in prep.).

Data points in between the two model series are consistent with a different combination of warm and cold components on top of the hot base model. Another effect that contributes to the spread of the sample is a different column density, as illustrated with one extra model from the 400 K series where we increase the column density by a factor 10, marked with a dashed red line in Figure 9. This model matches the direction of

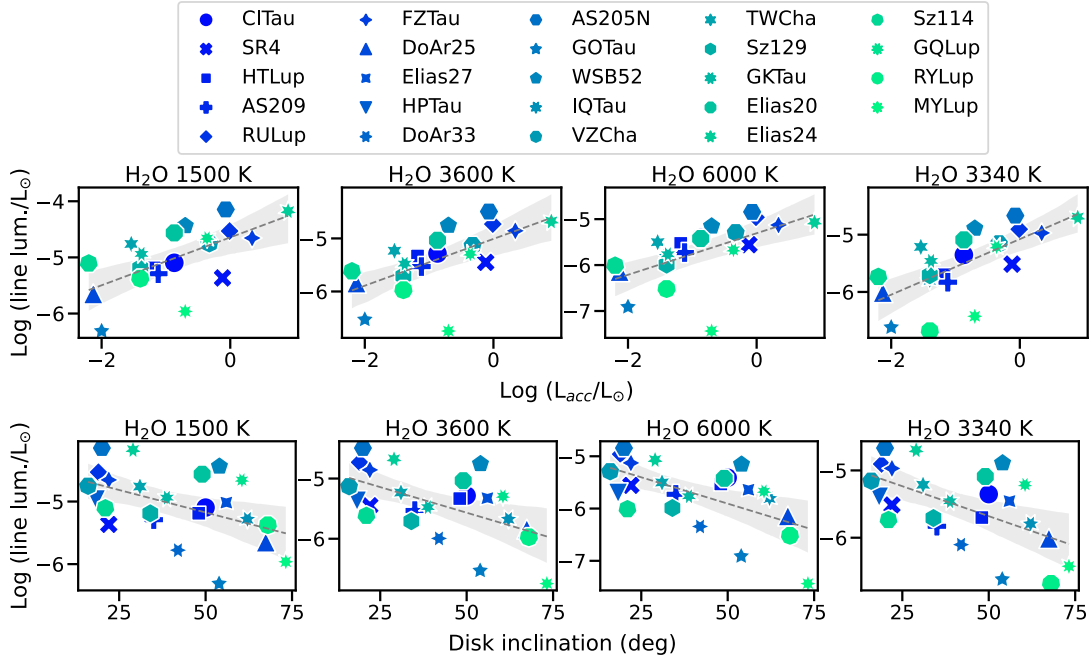


Figure 11. Trends between the water lines from Table 1 and the accretion luminosity (top) or disk inclination (bottom). Linear fits and their 95% confidence intervals are shown as dashed lines and shaded regions, and their parameters are reported in Appendix D.

spread in the data in the plot to the right, where the 3340 K line ratio decreases for increasing column density (as explained above). The sample analyzed in this work is consistent with having a factor of ~ 10 or more spread in column density of the 400 K component; the 170 K component does not contribute to the flux of the 3340 K lines because it is too cold (therefore the two model series overlap perfectly in the right panel of Figure 9), while the 850 K component has a much lower contribution to these lines than the 400 K component.

4.3. Trends with accretion, inclination, and disk size

In reference to previous work that found correlations in water emission as observed with Spitzer or ground-based instruments (Salyk et al. 2011; Banzatti et al. 2020, 2023a), it is important to test for correlations between the line fluxes and ratios used in Figure 9 and the accretion luminosity, one of the strongest correlations found before, and the disk inclination, for comparison to the inclination effects that will be shown later in Section 5. In Figure 11 we confirm with the new MIRI spectra that rotational water emission correlates with accretion and anti-correlates with disk inclination. The slope steepens with E_u in both cases, as found in Banzatti et al. (2023b) in the case of the correlation with accretion (linear correlation parameters are reported in Appendix D). For a previous discussion of these correlations in terms of inner disk heating and viewing angle effects, see e.g. Salyk et al. (2011); Banzatti et al.

(2023a,b). The water line ratios, instead, do not correlate with these properties (Figure 12), suggesting that the relative areas of emitting regions for water reservoirs at different temperatures are not set primarily by accretion and are independent of the viewing angle.

Another known correlation to test in the context of water emission from inner disks is with disk sizes as measured at high angular resolution with ALMA. In Figure 13 we show the trends between the three line ratios and the millimeter dust disk size following previous work (Banzatti et al. 2020, 2023b, see Appendix A for the millimeter data references). In this figure we include in the linear regression only the sub-sample of full disks with single stars, no millimeter inner dust cavities, and without signs of being in younger embedded phases (cloud/envelope contamination as reported in Andrews et al. 2018). The reason for this selection is to isolate the effects of gas and dust transport through the disk from other effects that may regulate the observed inner water vapor due to age and environment, inner disk depletion, and binary interactions (e.g. Salyk et al. 2024; Ramírez-Tannus et al. 2023; Perotti et al. 2023; Schwarz et al. 2024; Grant et al. 2024). These effects are being analyzed in upcoming papers.

The anti-correlations found in line ratios in the sub-sample of eight disks in Figure 13 correspond to what previously found in four disks in Banzatti et al. (2023b), which used a larger line list but similar energy levels. The correlation is detected only in the 1500/6000 K and

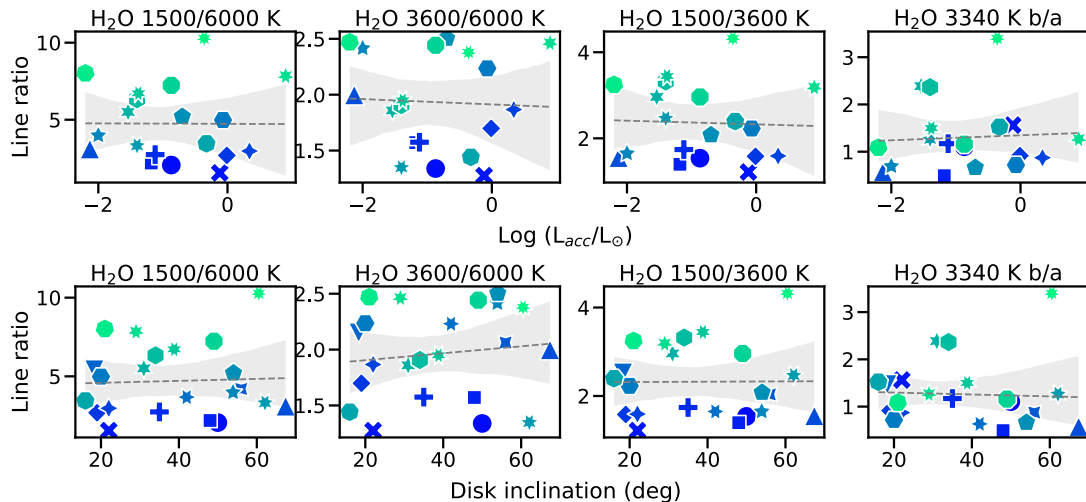


Figure 12. Same as Figure 11 but for the line ratios defined in Section 4. Linear fits and their 95% confidence intervals are shown as dashed lines and shaded regions. No significant correlations are found in these cases.

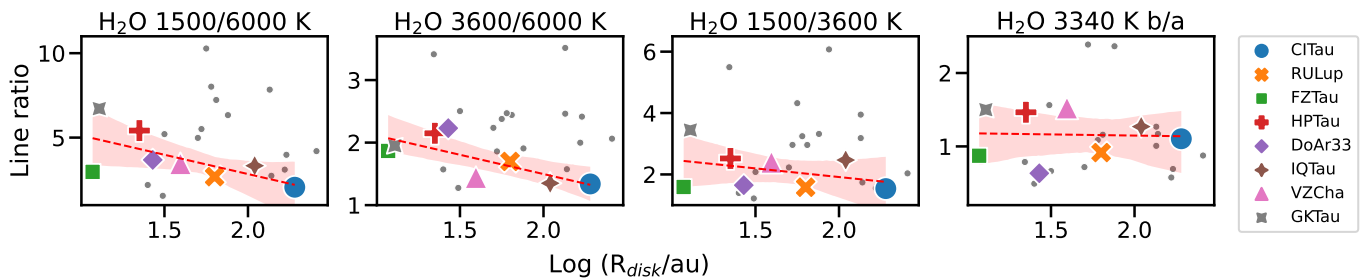


Figure 13. Correlations between the line ratios defined in Section 4 and the dust disk size as measured from ALMA images. Colored larger datapoints (used for the linear fit) show full disks with single stars, no millimeter cavity, and no cloud contamination. The rest of the sample is shown with small grey dots and is excluded from the fit. The first two correlations to the left correspond to what found in [Banzatti et al. \(2023b\)](#), which used a larger line list but similar energy levels. Linear fits and their 95% confidence intervals are shown as dashed lines and shaded regions, and their parameters are reported in Appendix D.

3600/6000 K line ratios, suggesting that the underlying physical process regulates the flux (here interpreted as emitting area) observed in the 170 K and 400 K water components relative to the hot inner water reservoir, which is instead mostly regulated by accretion ([Banzatti et al. 2023b](#)). The 3340 K line ratio, instead, does not correlate with disk size, suggesting that the column density of the 400 K component is independent from the underlying process driving this correlation. For a discussion of these trends in terms of pebble drift and other radial transport processes enriching inner disks with water vapor, see e.g. [Ciesla & Cuzzi \(2006b\)](#); [Najita et al. \(2013\)](#); [Banzatti et al. \(2020, 2023b\)](#); [Schneider & Bitsch \(2021\)](#); [Kalyaan et al. \(2021, 2023\)](#); [Mah et al. \(2024\)](#), [Houge et al. \(submitted\)](#).

The figures in this section are provided as future reference for fundamental dependencies of the observed line luminosities to system parameters, which will help interpreting water spectra of specific disks. Multiple factors play a role in driving the physical or chemical properties

of the water emitting regions in inner disks, and distinguishing their relative role in specific cases will not be trivial. However, based on previous work and Figure 11 we can expect that the water luminosity generally correlates with accretion, and with stronger correlation for higher-energy levels. We can also generally expect that the viewing angle plays a role in how we observe water spectra, with a luminosity that decreases at higher inclinations. As shown in Figure 12, instead, the line flux ratios are generally less dependent on accretion and inclination, suggesting that they may depend more on other processes.

5. GAS KINEMATICS IN MIRI SPECTRA

Building upon previous work, the diagnostic diagrams defined above in Section 4 and Figure 9 demonstrate that different disks have different fractions of temperature components in their inner disk, showing up as a different spectral line flux distribution where hotter emission populates higher- E_u and colder emission emerges

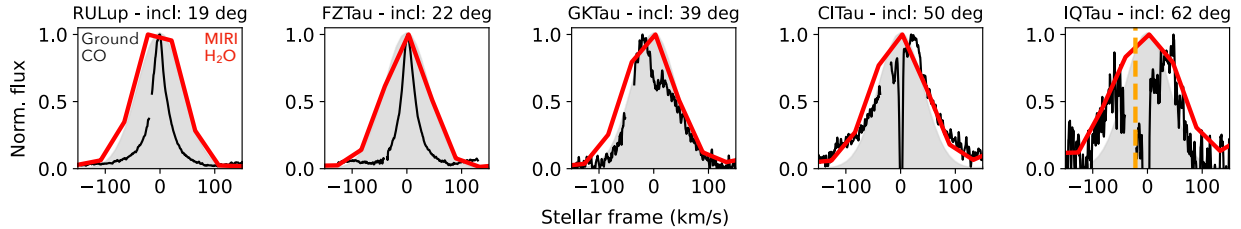


Figure 14. Evidence for disk-rotation Doppler broadening of molecular lines observed with MIRI-MRS. High-resolution ($R > 50,000$) ro-vibrational CO line profiles are shown in black (from [Brown et al. 2013](#); [Banzatti et al. 2022](#)). The single (un-blended) MIRI water line at $17.35766 \mu\text{m}$ ($E_u \sim 2400$ K, Appendix E) is shown in red. A gaussian broadening that assumes a resolving power equivalent to $\text{FWHM} = 95$ km/s is shown for comparison as a grey shaded area. The orange dashed line in IQ Tau shows the centroid of the blue-shifted absorption component found in the ro-vibrational lines in its MIRI spectrum (Figure 18).

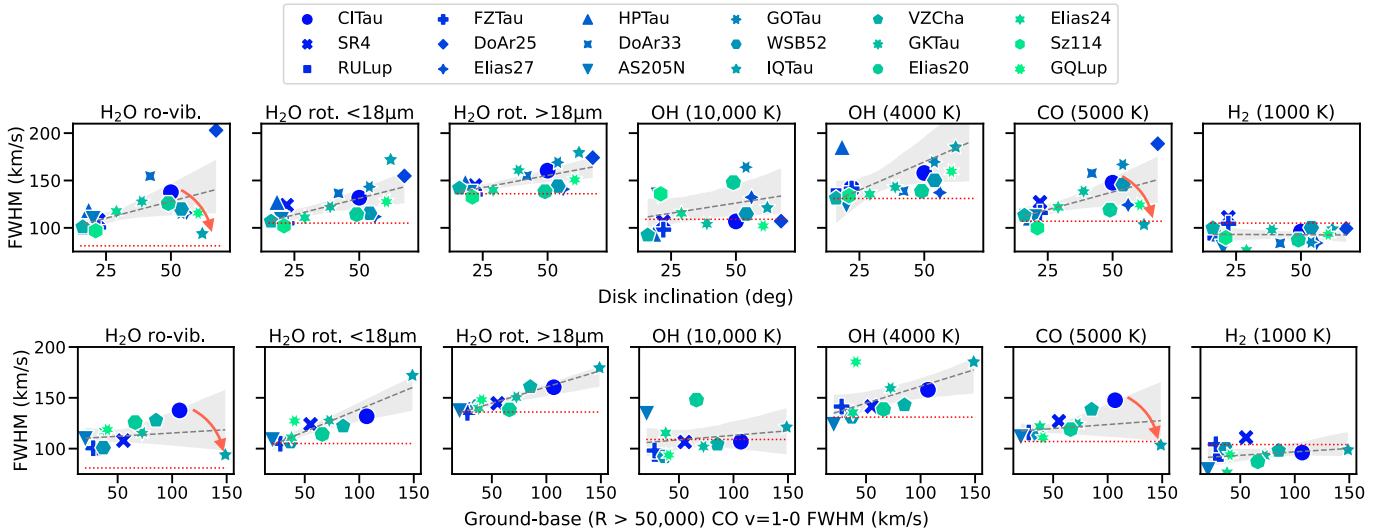


Figure 15. Evidence for disk-rotation Doppler broadening of molecular lines observed with MIRI-MRS. In this figure we exclude disks with inner dust cavities or lower S/N (see Appendices A and H). The observed line FWHM of H_2O , OH, and CO correlates with disk inclination (top) and with the high-resolution CO FWHM from ground-based observations where available (bottom). The nominal MIRI resolving power is reported as a horizontal dotted line for reference in each panel from [Pontoppidan et al. \(2024\)](#). The direction indicated with an arrow shows the effect of blue-shifted wind absorption observed in IQ Tau (Sect. 5.2). Linear fits and their 95% confidence intervals are shown as dashed lines and shaded regions, and their parameters are reported in Appendix D. The color-coding follows that of model series in Figure 9 as in Figure 11.

at lower- E_u to the extent to which it is present in a given disk. This is consistent with results from ground-based higher-resolving-power spectra, which additionally measured a gradient in line widths with broader higher-energy lines and narrower lower-energy lines directly demonstrating a temperature gradient across disk radii (see Figure 13 in [Banzatti et al. 2023a](#)). The recent characterizations of the resolving power of MIRI ([Argyriou et al. 2023](#); [Pontoppidan et al. 2024](#)) now open the way to test whether some water lines may be partially spectrally resolved. If this is true, we could determine their orbital region (not just the equivalent emitting area provided by the slab models used so far to fit MIRI spectra) from the observed kinematics and improve estimates of the radial distribution of water suggested by the line flux ratios in the previous section.

In this section we present the detection and a first general analysis of disk-rotation Doppler line broadening measured in MIRI spectra. Even in this case, the list of single un-blended lines presented in Section 3 turns out to be very important to provide the most reliable measurements of line widths across MIRI wavelengths.

5.1. Doppler broadening of emission lines

Potential inclination effects on the observed MIRI spectra were pointed out in [Banzatti et al. \(2023b\)](#) in the case of the high-inclination (62 deg) disk of IQ Tau, which showed broader lines than the nominal resolving power and a more compact slab emitting area than in three other disks. In reference to this finding, Figure 14 shows the single water line at $17.35766 \mu\text{m}$ ($E_u \sim 2400$ K) for selected targets where

high-quality ro-vibrational CO lines are available at high resolving power from ground-based spectrographs. The figure demonstrates that, just like the high-resolution CO lines, the MIRI water lines also become broader at higher disk inclinations, suggesting a similar effect of rotational Doppler broadening from gas in the disk. By extending the sample and systematically measuring the line widths in all disks we can now conclusively test Doppler broadening as a general effect in MIRI spectra.

Figure 15 presents clear evidence for disk-rotation Doppler broadening of line widths measured with MIRI. For water, we split the measured line widths (using the same line list presented above and reported in Appendix E) into three panels: one for ro-vibrational lines at $< 9\mu\text{m}$, one for rotational lines at $< 18\mu\text{m}$, one for rotational lines at $> 18\mu\text{m}$. In each case, we show the median FWHM value measured in each disk to capture a representative line broadening in each wavelength range. The top panel shows the line FWHM against disk inclination, which should show a positive trend when lines are broadened by Keplerian rotation in a similar inner disk region as observed from a range of viewing angles. The bottom panel shows the FWHM of MIRI lines against the FWHM of $v = 1 - 0$ CO lines measured at much higher resolving power ($R > 50,000$) with ground-based spectrographs in previous surveys (Brown et al. 2013; Banzatti et al. 2022), which should correlate if they are both broadened by Keplerian rotation in the inner disk. High-resolution spectra from the ground already showed that CO and H₂O lines share a similar shape and broadening at 4.6–12.4 μm (for an overview, see Banzatti et al. 2023a), and the correlations now found with line widths from MIRI spectra extends this finding to wavelengths of $> 13\mu\text{m}$. At the lowest disk inclinations, the narrowest lines are consistent with the nominal MIRI resolving power (except for the ro-vibrational lines) as measured in previous work (Argyriou et al. 2023; Pontoppidan et al. 2024), which is reported in each panel of the figure for comparison. In the case of the three water emission ranges illustrated in the figure, we show median values of the nominal resolving power of MIRI over the relevant wavelength ranges.

For comparison to the H₂O lines, Figure 15 reports the trends observed in a single hot OH line at 14.62 μm ($E_u \sim 10,754$ K, the only single OH line we can find at MIRI wavelengths, which may include some contamination from organics depending on the relative strength), a lower-energy OH line pair that overlaps in wavelength at 23.05 μm (with $E_u \sim 4100$ K), the P26 line of $v = 1 - 0$ CO emission (one of the only three un-blended CO lines in MIRI spectra with minimal contamination from water and other higher-energy CO vibrational lines, to-

gether with P25 and P27), and the H₂ S(1) line near 17 μm , which is well separated from emission from other molecules (see Figure 3). While water, CO, and partly OH show similar evidence for Doppler broadening, supporting their disk origin, the H₂ line width does not increase with inclination, suggesting that the line is typically unresolved. Another H₂ line that can be measured is the S(3) line at 9.665 μm (Figure 2); this line too provides evidence for being unresolved in MRS spectra (Figure 16), but it is blended on each side with H₂O and OH lines which can contaminate its measured FWHM in some cases (e.g. FZ Tau). The other H₂ lines covered by MRS are all blended with H₂O but still consistent with the local resolving power at each wavelength. That H₂ is unresolved in MRS spectra is consistent with a non-disk origin for H₂ emission, which is indeed observed to trace outflows and winds in young disks (e.g. Yang et al. 2022; Arulanantham et al. 2024; Delabrosse et al. 2024). Another option could be extended emission from larger disk radii (therefore narrower lines) than the emission from other molecules detected in MIRI spectra.

5.1.1. Updates on the MIRI resolving power

The data in Figure 15 show that the narrowest lines are found at low inclinations, as expected from Keplerian broadening. We can therefore use MIRI spectra of low-inclination disks to measure the MIRI resolving power, as done recently in Pontoppidan et al. (2024). This is done in Figure 16, where three targets are selected for their low inclination (FZ Tau, 22 deg, and RU Lup, 19 deg) and low stellar mass (Sz 114, 21 deg, 0.2 M_\odot), which provide the best conditions to have unresolved lines across the MIRI spectrum. Their line measurements are shown in reference to the MIRI resolving power from Argyriou et al. (2023), which used HI and forbidden lines from a planetary nebula, and Pontoppidan et al. (2024), which used water and CO lines from the protoplanetary disk of FZ Tau.

The characterization from Pontoppidan et al. (2024) is confirmed overall, including the much higher resolving power in channel 4 in comparison to what was estimated in Argyriou et al. (2023). In this new analysis we identify a few sub-bands where the resolving power is slightly better than what was previously found in Pontoppidan et al. (2024), and we provide the updated profile in Figure 16 (the red dashed line) and tabulated in Table 4 of Appendix C. In particular, we identify the H₂ line at 17.035 μm as providing a useful anchor point showing a higher resolving power than what the nearby water lines show, suggesting that these might be partially resolved in disks. By taking the median value of measurements for this H₂ line in this sample, we estimate

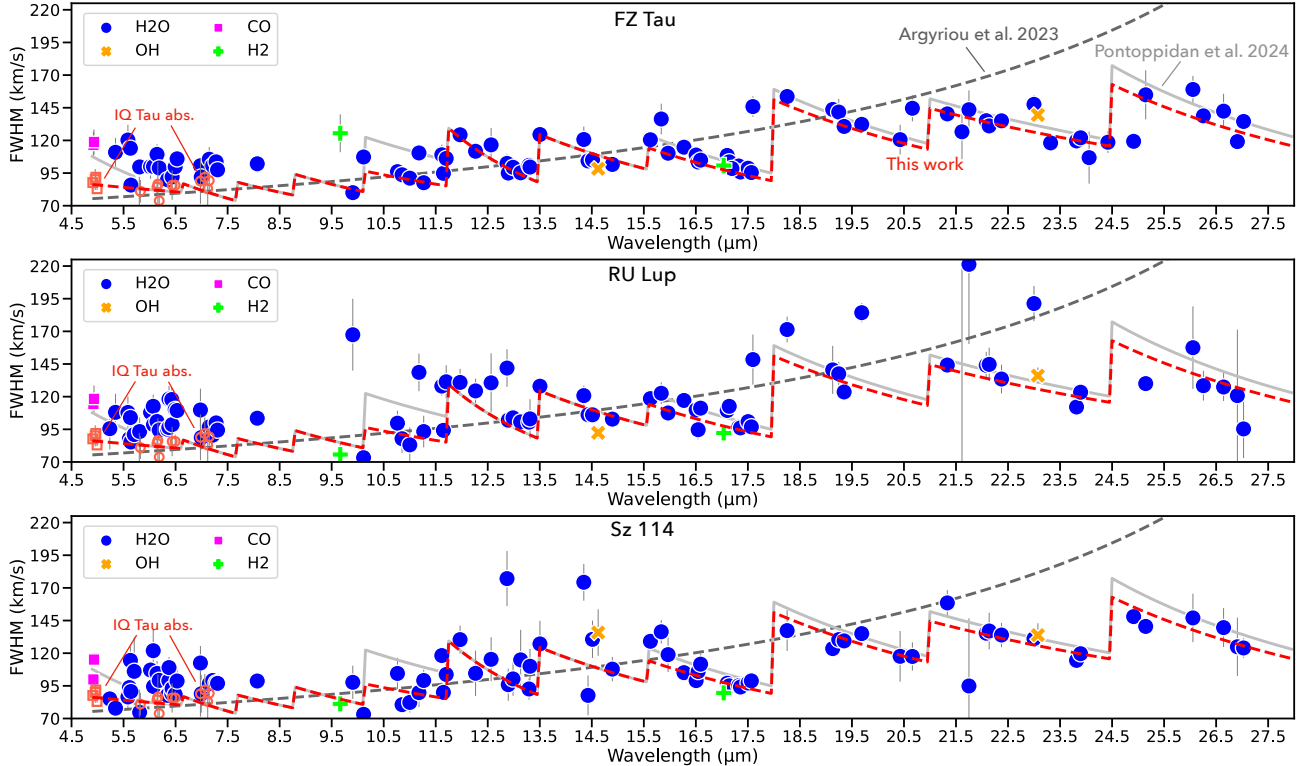


Figure 16. MIRI-MRS resolving power from line width measurements in this work, as compared to recent works (Argyriou et al. 2023; Pontoppidan et al. 2024, gray dashed and solid lines, respectively). The unresolved H₂ lines (light green crosses) provide useful anchor points suggesting a slightly better resolving power near 17 μm (see also Figure 15) than what was estimated in Pontoppidan et al. (2024), and the absorption lines in IQ Tau (light red open datapoints) demonstrate that the resolving power at the shortest wavelengths is consistent with what was estimated in Argyriou et al. (2023). The resolving power we adopt in this work is shown with a red dashed line (see Table 4 in Appendix C and Pontoppidan et al. (2024)).

$\text{FWHM}_{\text{MRS}} \sim 93 \text{ km/s}$, i.e. about $\sim 10 \text{ km/s}$ better than what was estimated in Pontoppidan et al. (2024) at this wavelength.

5.1.2. Doppler broadening as a function of E_u

Another very interesting trend emerges from considering line broadening as a function of upper level energy E_u . This can be easily analyzed over small spectral ranges where the resolving power is approximately constant, to avoid confusing the signal with a changing resolving power with wavelength. This was one of the reasons why we selected lines between 14.4 and 17.6 μm in Section 3.2: the resolving power is approximately the same (see Figure 16) and there is a good number of single (un-blended) lines that can be used for FWHM measurements. If water emission comes from a radially narrow region that can be well approximated with a single temperature component, we should not expect an observable trend between the measured line FWHM and E_u . To the contrary, if water emission comes from a more extended disk region that has a larger temperature gradient, we may be able to measure a trend between

FWHM and E_u , where the lower- E_u lines should become increasingly narrower.

This is exactly what is observed in the data when comparing two disks that have previously been proposed to be in these two different situations: Figure 17 shows that the spectrum of GQ Lup, with one of the strongest and most extended cool water components found so far, has a clear trend between FWHM and E_u , while the same lines in CI Tau are flat with E_u . The rest of the sample is shown in Appendix F. This finding provides new, independent confirmation of previous work that proposed water to trace an extended disk region in disks with increased emission from low-energy lines (Banzatti et al. 2023b; Muñoz-Romero et al. 2024a). Line broadening will be applied in Section 6 to extract radial profiles from the observed water emission.

5.2. Water and CO absorption at high inclinations

If lines observed with MIRI-MRS are rotationally broadened at high inclinations as demonstrated in the previous section, we could also expect to observe absorption on top of emission lines with different Doppler broadening, since this is observed at high-resolution

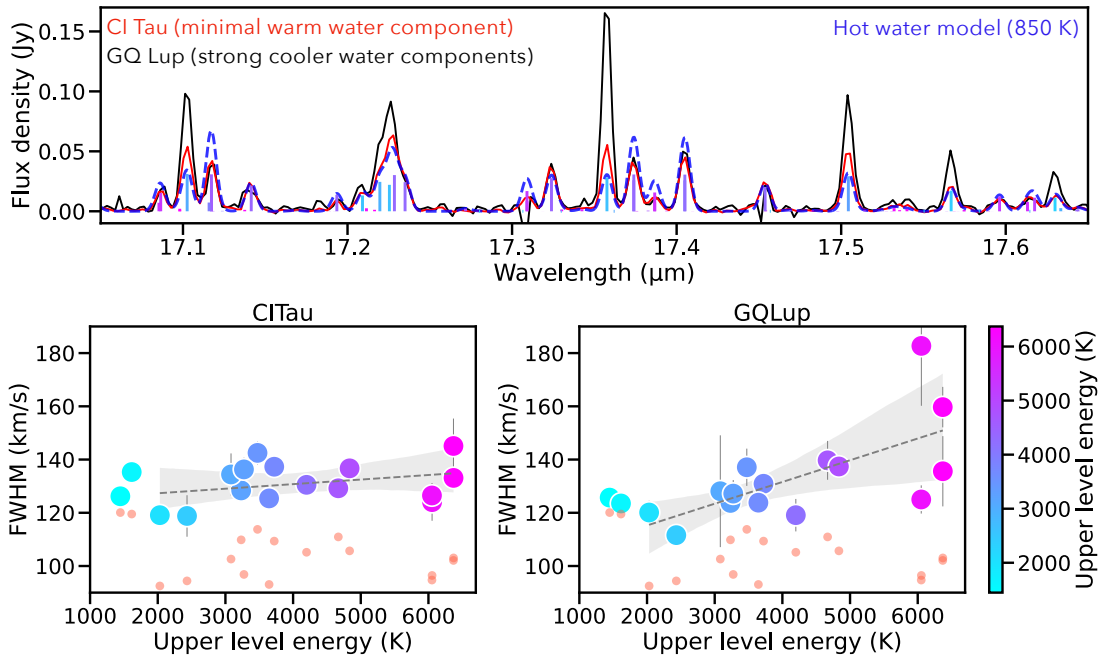


Figure 17. Evidence for Doppler broadening of MIRI water lines as a function of upper level energy E_u . The figure includes the same two disks that have minimal warm water component (CI Tau) vs a strong cold water component (GQ Lup) as defined in Section 4; the rest of the sample is included in Appendix F. In the upper panel, their spectra are scaled as in Banzatti et al. (2023b) and show individual transitions as in Figure 3. The water lines in GQ Lup become narrower at lower E_u , as expected if the cold water reservoir is in a disk region at larger radii (Banzatti et al. 2023b; Muñoz-Romero et al. 2024a). Light red dots show the updated MIRI resolving power at each line wavelength from Figure 16. The two lines near 1500 K from Table 1 are excluded from the fit, due to the lower resolving power at 23 μm .

from the ground (e.g. Pontoppidan et al. 2011; Brown et al. 2013; Banzatti et al. 2022, 2023a). The best test case should be a high-inclination disk with deep blue-shifted absorption observed in ro-vibrational CO emission from the ground, since absorption is observed to deepen at higher disk inclinations possibly due to a larger portion of an inner disk wind intercepted along the line of sight (Pontoppidan et al. 2011; Banzatti et al. 2022). In our sample this is the case of IQ Tau, whose CO ro-vibrational line shape shows broad double-peaked emission (due to its high inclination of 62 deg) with at least one blue-shifted absorption component (Figure 14, previously shown in Brown et al. (2013)).

Figure 18 shows portions of the ro-vibrational CO and H₂O spectra from the MIRI spectrum of IQ Tau, confirming the scenario proposed above. The spectral lines of both molecules show a broader and more complex shape than in other disks in this work, a shape that can be excellently matched with the simple difference of two spectra: a hotter spectrum in emission at the RV of the star (with FWHM = 150 km/s, much larger than the nominal resolving power at these wavelengths, as already shown in Figure 15), and a colder spectrum blue-shifted by -7 km/s (with FWHM = 80–90 km/s); the models used for absorption adopt a similar column

density of $1\text{--}5 \times 10^{17} \text{ cm}^{-2}$. While the models in this figure are just for quick demonstration, we remark that the data seem to clearly show two aspects: that the absorption spectrum is blue-shifted, and that it is cooler than the emission spectrum. The different temperature is most evident from the $v = 2 - 1$ CO lines, which are less absorbed than the $v = 1 - 0$, and in the water lines, where it is the low-energy lines to have the most significant absorption (see color-coded E_u transitions in Figure 18).

This finding opens up the possibility to distinguish and study blue-shifted absorption from inner disk winds in molecular disk spectra observed with MIRI. At the same time, it highlights the importance of having high-resolution molecular spectra from ground-based instruments, that easily distinguish absorption and blue-shifted winds in the velocity-resolved line profiles (for a recent overview, see Banzatti et al. 2022), to support the analysis of MIRI spectra. The detailed analysis of the molecular wind absorption spectrum in IQ Tau and other disks is left for future work. For a detailed discussion of the analysis of water absorption spectra as observed with MIRI-MRS, see Li et al. (2024).

One immediate practical application in this work is that we can use measurements of absorption lines in

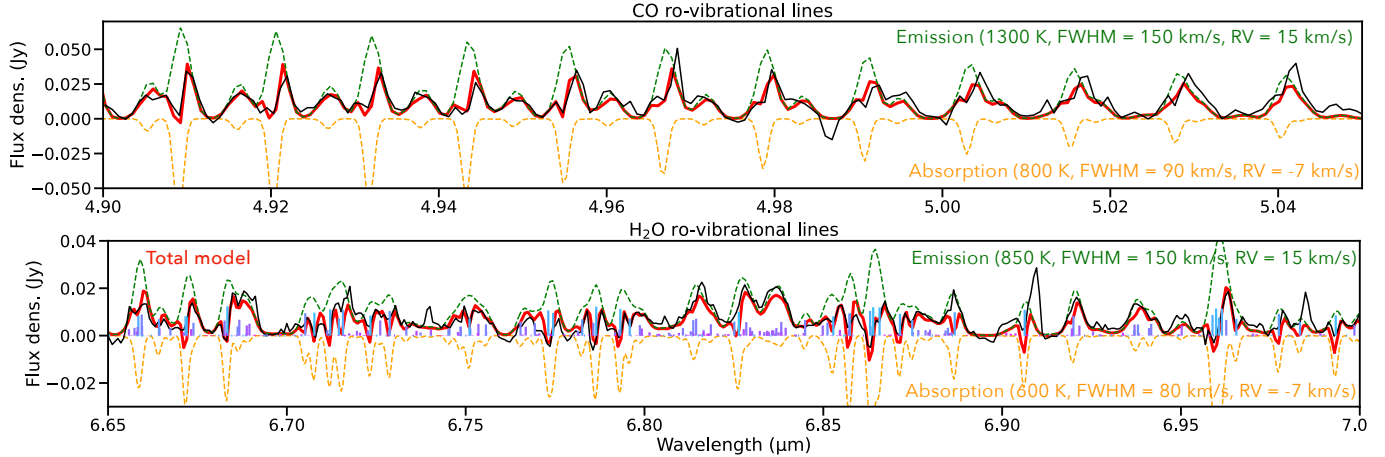


Figure 18. Absorption spectra of ro-vibrational CO (top) and H₂O lines (bottom) in the high-inclination disk of IQ Tau. Two models with different RV, temperature, and FWHM are shown in the figure to approximately reproduce the data. The MRS data is shown in black, the difference of the two models in red. Individual water transitions are color-coded as in Figure 1, to illustrate that absorption is prevalent in lower-energy lines (cyan).

IQ Tau, which have FWHM of ≈ 7 km/s (Banzatti et al. 2022) and are therefore surely unresolved with MRS, to improve the characterization of the MIRI resolving power at the shortest wavelengths. This is shown in Figure 16, where we add with empty red datapoints the measured FWHM of absorption lines from IQ Tau. These confirm that the resolving power is close to that estimated in Argyriou et al. (2023), and demonstrate that ro-vibrational CO and H₂O emission lines are generally partially resolved by the MRS in protoplanetary disks, consistent with their small emitting radius obtained from the large line broadening observed at high resolution from the ground (Banzatti et al. 2023a).

A decrease in ro-vibrational line broadening was in fact visible even in Figure 15 in disks at inclinations > 50 deg (region marked with a red arrow), with IQ Tau providing the most extreme case where CO and H₂O lines decrease down to the MIRI resolving power. This suggests that ro-vibrational CO and H₂O absorption may be present and observable in MIRI spectra in disks at inclinations > 50 deg, which should be checked when the ro-vibrational lines are to be analyzed. In this sample, in addition to IQ Tau absorption seems to be visible in GQ Lup and possibly Elias 20 and GO Tau. In case high-resolution spectra from the ground are available, they can provide useful guidance on whether to expect absorption to be present in a specific disk; however, ground-based observations are not always available nor possible for MIRI targets. Cases where absorption is not as significantly blue-shifted as in IQ Tau (Figure 14), e.g. CI Tau, may only result in weaker lines and not be easily detected from the MIRI spectra alone (see previous discussion in Banzatti et al. 2023a).

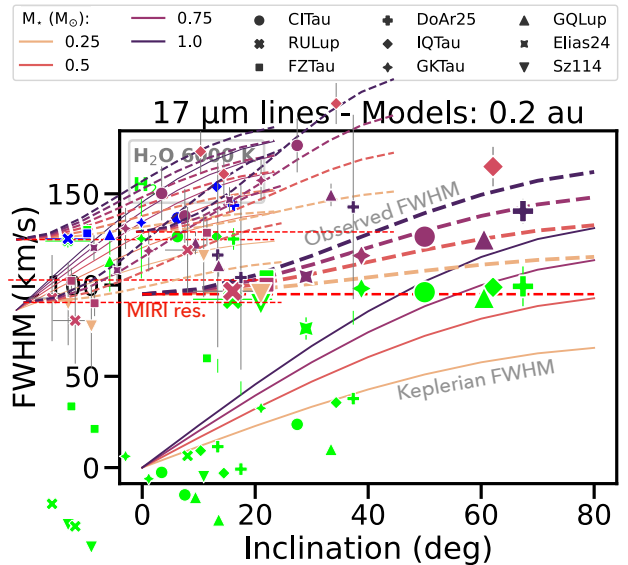


Figure 19. Keplerian interpretation for the Doppler broadening of emission lines in MIRI spectra. Line widths from Keplerian models at 0.2 au (with $\text{FWHM} = 2V_{\text{Kep}}$) are shown with solid lines for a range of stellar masses between 0.25 and $1 M_{\odot}$, their convolution to the MIRI resolving power is shown with dashed lines. For illustration, we show a selection of disks spanning the whole range in disk inclinations included in this work, and we use the 6000 K line from Table 1. The H₂ line at $17.035 \mu\text{m}$ is included as a reference for the MIRI resolving power (see Figure 16).

6. DOPPLER MAPPING OF MIRI WATER LINES

The data shown in Section 5 and Figures 14, 15, and 17 demonstrated that individual molecular lines in MIRI-MRS spectra may be rotationally broadened beyond the MIRI resolving power (except for H₂), depending on the disk inclination and the upper level

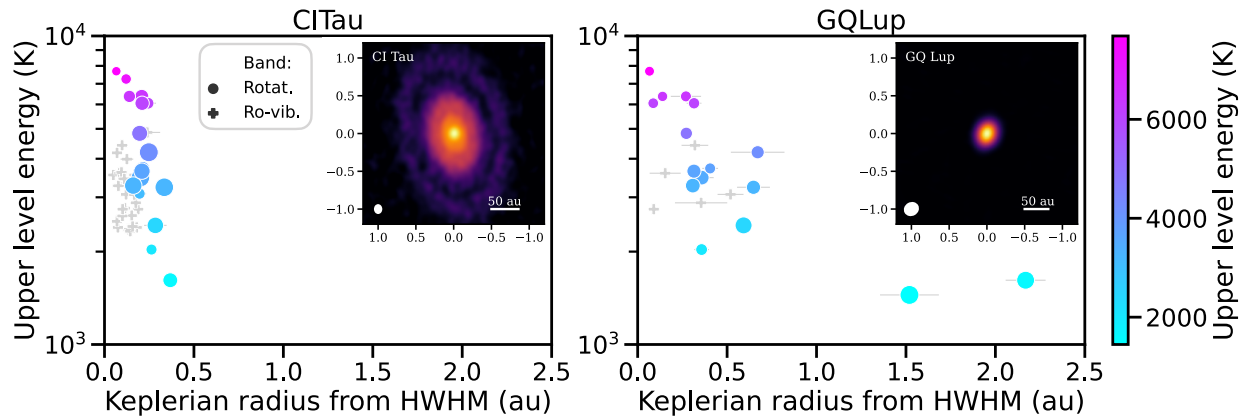


Figure 20. Radial profiles of water rotational lines observed in CI Tau (large, multi-gapped disk dominated by a single hot water component) and GQ Lup (compact disk with strong warm and cold water components), by applying the simple Doppler mapping technique described in Section 6 and Figure 19. ALMA continuum images are shown for reference in each panel (Long et al. 2019, and in prep.). All lines are partially resolved in both disks, enabling estimates of emitting radii from the de-convolved line broadening. Rotational lines are shown as filled circles with size proportional to the line flux (to illustrate the different spectral line flux distribution as in the top panel of Figure 8), ro-vibrational lines with grey crosses. Ro-vibrational lines in GQ Lup ($\text{incl} = 60$ deg) are very weak and possibly include absorption (see discussion in Section 5.2).

energy of the emitting lines. This finding, in addition to the strong correlations with the FWHM of ro-vibrational CO lines as observed from the ground at high resolving power, supports the idea that MIRI lines are rotationally-broadened by Doppler effect in an inner disk with an inside-out temperature gradient. In this section, for simplicity we assume that the Doppler broadening can be simply described by Keplerian rotation in the disk; for an overview and discussion of the possible contamination by a slow disk wind to the narrow CO components see Pontoppidan et al. (2011); Banzatti et al. (2022).

In Figure 19, we illustrate one example of how Keplerian rotation in the disk broadens MIRI lines beyond the resolving power. With solid lines we show the FWHM produced by gas in Keplerian rotation at 0.2 au (which should be appropriate for high-energy lines, see overview in Banzatti et al. 2023a) for a range of stellar masses between 0.25 and 1 M_{\odot} . With dashed lines, we show how the Keplerian models would be observed after convolution with the MIRI-MRS resolving power, by assuming $\text{FWHM}_{\text{obs.}} = \sqrt{(\text{FWHM}_{\text{MRS}})^2 + (\text{FWHM}_{\text{Kepl.}})^2}$. We do not include any thermal broadening component, as it is completely negligible (< 5 km/s) at the temperatures relevant for this work (< 1000 K, see e.g. Meijerink et al. 2009; Pontoppidan et al. 2024; Muñoz-Romero et al. 2024a). As can be seen from the models, Doppler broadening should become detectable in high-S/N spectral lines starting at inclinations as low as ~ 20 deg, especially in disks around stars with larger mass.

For comparison to the models, we include the 17.32 μm ($E_u \sim 6000$ K) line from Table 1 tracing hot water emission for a representative sample of targets

that spans the entire range in disk inclinations included in this work, with masses between 0.2 and 1 M_{\odot} (color-coded in the same way as the models, for comparison). This line is confirmed to be consistent with tracing disk radii at ~ 0.2 au in a few disks that overlap with their stellar-mass model curve (e.g. CI Tau); instead, disks falling above their stellar-mass curve indicate emission from smaller radii (IQ Tau) and those falling below indicate emission at larger radii (GQ Lup). For reference, we also show the H_2 line that reflects the MIRI resolving power near 17 μm (Section 5.1.1).

The simple Doppler mapping technique illustrated in Figure 19 is generally applied to multiple MIRI lines in Figure 20, providing a radial excitation profile with line upper level energies as a function of their Keplerian emitting radius from the line broadening. In this figure, as examples we include two disks that were previously identified to have a hotter and supposedly more compact versus a colder and supposedly more extended emission, the same disks shown in Figure 17. Here we use the line $\text{FWHM}/2 = \text{HWHM}$ (for the Keplerian velocity V_{Kepl} from one side of the disk) as de-convolved with the local MIRI resolving power (Section 5.1.1), for the same sample of lines used for Figure 17. This radial excitation profile provides a new demonstration, completely independent from the temperature fits made in previous work, for the different spatial distribution of water in these two disks: in CI Tau (large, multi-gapped disk dominated by a single hot water component, proposed to have a reduced icy pebble drift) confined within $\lesssim 0.3$ au, and in GQ Lup (compact disk with strong warm and cold water components, proposed to have a stronger water enrichment from pebble drift) extending

out to > 1.5 au. For a discussion of the different temperature and radial distribution of water in these two disks in the context of pebble drift delivering water to the inner disk, see [Banzatti et al. \(2023b\)](#) and [Muñoz-Romero et al. \(2024a\)](#).

An important caveat to consider is that these regions are derived from the line broadening (which can be measured in MIRI spectra) and only provide a characteristic emitting radius that does not reflect the full radial extent of the emission, which would be shown from the velocity of the typical double peaks from Keplerian rotation (which instead cannot be measured in MIRI spectra). However, these Keplerian radii estimated from MIRI spectra can be used for relative comparisons between different disks. The two examples shown in [Figure 20](#) qualitatively confirm the relative difference in line emitting regions estimated from temperature-gradient fits to the line fluxes in [Muñoz-Romero et al. \(2024a\)](#), highlighting the potential in future work to improve model fits to MIRI spectra by including both line excitation and line broadening. These radial excitation maps are also valid for comparing the relative emitting region of different lines in a given disk; for instance, CI Tau shows that ro-vibrational lines are emitted from smaller disk radii than the rotational lines. This is consistent with what higher-resolution spectra from the ground have recently shown ([Banzatti et al. 2023a](#)).

7. DISCUSSION

In this section we will discuss some applications of the tools and findings presented above to study MIRI water spectra in protoplanetary disks, with the intent to provide a helpful framework for community efforts and a common ground for comparisons of different samples.

7.1. Combining flux and broadening information

The diagrams in [Figure 9](#) have been introduced for providing a simple, general view of the relative emission from water at different temperatures in different disks. This simple diagnostic can provide a helpful starting point before performing detailed fits with slab or more sophisticated models, and provides an empirical framework for comparisons across different datasets independently from different tools that may be used in different works. The position of a given disk in these diagrams informs on whether a ~ 400 K and ~ 170 K components significantly contribute to its water spectrum, and on the column density of a ~ 400 K component. These temperature components are only a convenient approximation of a temperature gradient that is found in disks ([Muñoz-Romero et al. 2024a](#); [Timmink et al. 2024](#)), and they could in principle probe physical gradients both in the radial and vertical direction in an inner disk surface.

As demonstrated in [Section 5.1](#), the detection of Doppler broadening of MIRI lines can help clarify the interpretation of the position of a given disk in [Figure 9](#) in terms of the radial distribution of water. As shown in [Figure 20](#), a disk like CI Tau that sits close to the 1,1 point in the diagram has compact emission from an inner, hotter disk region that can describe the observed emission from a large range of E_u , with only a slightly larger emitting radius for the lower $E_u \sim 1500$ K. This explains why it has been found in previous work to be well reproduced by a single hot temperature component ([Banzatti et al. 2023b](#); [Muñoz-Romero et al. 2024a](#)). To the contrary, a disk like GQ Lup that sits along the warm+cold model series shows a gradient in line widths that corresponds to a much larger range of disk radii, with higher E_u emitted from an inner region and lower E_u emitted from significantly larger radii. This was generally expected from disk models and velocity-resolved surveys ([Figure 13](#) in [Banzatti et al. 2023a](#)), but had never been directly observed from the broadening of water lines at $> 13 \mu\text{m}$ before this work.

We now combine the flux and broadening measurements from MIRI spectra into [Figure 21](#), for the subsample of disks in this work where Doppler broadening is detected across all energy levels ([Appendix F](#)). The figure shows the ratio of Keplerian radii (each radius obtained from the deconvolved HWHM as in [Figure 20](#)) as a function of their line flux ratio, for the characteristic E_u values considered above in this work. To use a representative Keplerian radius for each E_u , we take the median radius of lines included in [Figure 20](#) for each of these ranges: 1400–1700 K, 3000–4000 K, and 6000–6500 K. [Figure 21](#) shows the example of the 1500/6000 K line ratios (their flux ratio and Keplerian radius ratio), which maximizes the range of values measured in spectra (as the cold component is generally more distant from the hot component). With the exception of IQ Tau (the same high-inclination disk where wind absorption is detected, see [Section 5.2](#)), the trend in this figure shows that a higher line flux ratio generally corresponds to a larger emitting radius of the cold component, supporting the model tracks we have used above in [Figure 9](#) where it was the emitting area to increase. Therefore, the line broadening measurements support the idea that [Figure 9](#) can be generally used to obtain a quick reference for the radial distribution of water in the inner disk in three temperature regions, which we illustrate with a cartoon in the right panel of [Figure 21](#), adapted from [Banzatti et al. \(2023b\)](#). In addition to the approximate distribution of these temperature components, the 3340 K line flux ratio introduced in [Figure 9](#) provides a proxy for the column density in the warm region, as explained above.

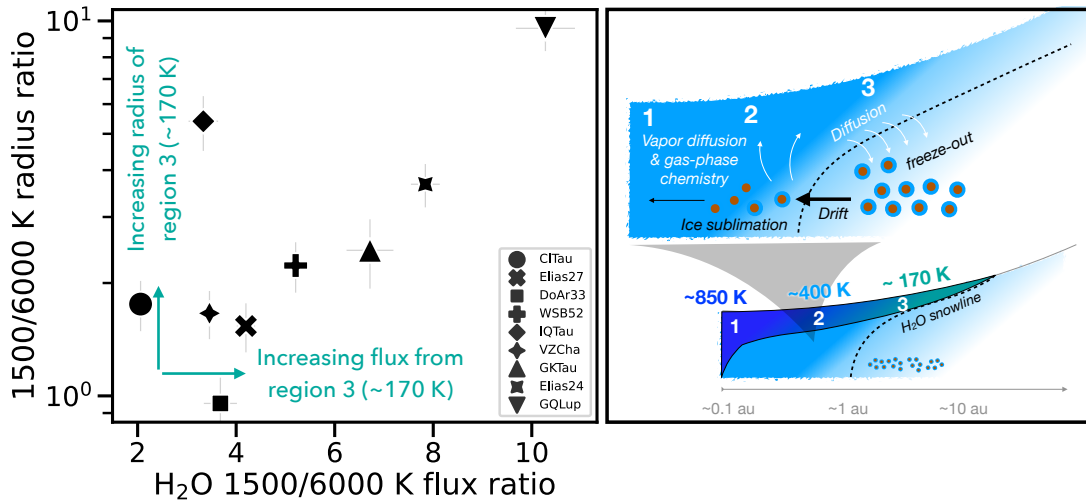


Figure 21. Left: Ratios of Keplerian radii estimated from the deconvolved line widths (Figure 20) as a function of their line flux ratio, using the 1500 and 6000 K lines from Table 1. This figure includes only disks where Doppler broadening is detected (Appendix F). With the exception of IQ Tau, the disk where wind absorption is detected (Figure 18), the trend in this figure shows that a larger flux in the 1500 K lines corresponds to their larger Keplerian radius too. Right: illustration of the three temperature regions at increasing disk radii and processes of ice drift, sublimation, and gas diffusion, modified from Banzatti et al. (2023b).

To analyze more comprehensively the water abundance near and across the snowline at a temperature of 170 K and below, instead, access to lower-energy levels at $> 30\mu\text{m}$ will be needed (e.g. Zhang et al. 2013; Blevins et al. 2016; Banzatti et al. 2023b), which would be provided by a future far-infrared observatory (Pontoppidan et al. 2018, 2023; Kamp et al. 2021). Dynamic disk models including dust evolution and water processing are beginning to unfold how the observable water columns can evolve with time under the effect of pebble drift (see, e.g., Houge et al. submitted). Generating synthetic spectra and evolutionary tracks of such models in the context of the diagnostics presented in Figure 9 will be the subject of future work. Here we note that by taking the cold water mass values from the model track in Figure 9 and converting those into a pebble mass delivered to the snowline using Eqn. 11 from Muñoz-Romero et al. (2024a) gives pebble mass fluxes between 0.6 and $5 \text{ mM}_{\oplus} \text{ yr}^{-1}$, consistent with typical predictions from dust evolution models (e.g. Drazkowska et al. 2021).

7.2. A procedure for the analysis of water spectra

We propose now in Figure 22 a simple general procedure for the analysis of water spectra, by combining the findings and tools presented above to the list of guidelines provided recently in Banzatti et al. (2023a), which was based on lessons learned from ground-based surveys of water emission from protoplanetary disks.

7.2.1. Step 1 - Spectral line inspection

The first step after reducing the spectra and subtracting the continuum (see Appendix B for guidelines on

that step) is to inspect them carefully across MIRI wavelengths for the general identification of a series of properties. These properties, related to line blending and excitation, will be useful and in some cases fundamental for a correct analysis of water emission to study physical and chemical processes in inner disks.

Relative emission in high- vs low-energy lines—With guidance from the atlas presented in this work, the identification of the general distribution of water temperature components can be visualized from the relative ratio of lines dominated by higher- E_u versus lower- E_u . The $16\text{--}18 \mu\text{m}$ range is well suited for the hot and warm components, by including lines with E_u from above 6000 K down to 2000 K (Figure 4 in Banzatti et al. (2023b) and Figure 17 in this work). The best lines at MIRI wavelengths where colder emission consistent with the snowline region emerges are two transitions around $23.85 \mu\text{m}$ (Zhang et al. 2013; Banzatti et al. 2023b; Muñoz-Romero et al. 2024a; Temmink et al. 2024), including their relative asymmetry which at lower temperatures is prominent in a stronger 1448 K line at $23.82 \mu\text{m}$ (Figure 8). This will give a first general impression of the global water distribution in the inner disk of a given target or sample, see e.g. Appendix H for the sample in this work.

Contamination from other species—Next, before water emission lines shall be extracted and used for analysis, the atlas can be used for general reference of contamination from other species. To evaluate that carefully on individual targets, models that at least approximately

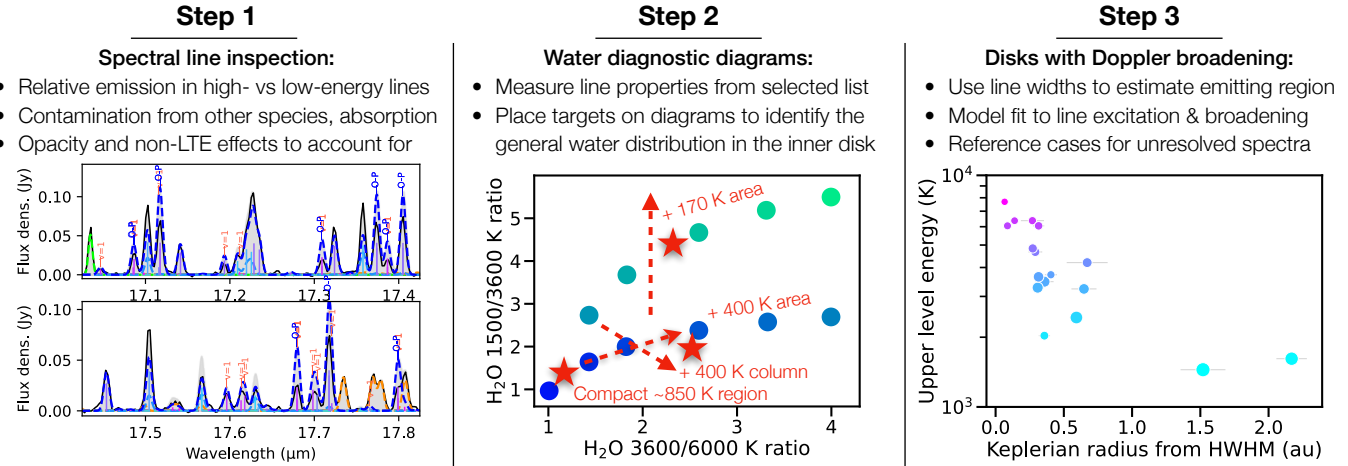


Figure 22. General procedure for the analysis of water spectra based on the findings and analysis presented in this work.

reproduce the observed emission from other molecules should be used, as done in the example of CI Tau in Figures 1 to 4. With this process, it is possible to identify which water lines can be extracted and used for analysis without having to subtract other emission models. In this work we provide a curated list of single un-blended lines that should provide the most reliable measurements in most situations (Section 3); in case of weak water relative to organic emission, lines at 12–16 μm should be checked for contamination and possibly removed from the list.

Absorption—If high-resolving-power infrared spectra are available from ground-based instruments, those can be used to check for the presence of absorption in the ro-vibrational lines. If not, the MIRI spectra at $< 9 \mu\text{m}$ should be inspected to identify potential blue-shifted absorption (e.g. Figure 18), especially disks observed at inclinations $> 50 \text{ deg}$ (Figure 15) that may generally have blue-shifted absorption by intercepting an inner disk wind (Pontoppidan et al. 2011; Banzatti et al. 2022). Identifying absorption solely from MIRI data needs a strong absorption blue-shift and a broad emission component and will likely be possible only in a limited number of cases. Ground-based observations demonstrate that absorption is rather common in ro-vibrational CO spectra and may be blended into emission producing weaker line fluxes in MIRI spectra (Figure 15 in Banzatti et al. 2023a), making their interpretation more challenging. In those cases where the absorption blue-shift is large enough to enable detection in MIRI spectra, the ro-vibrational lines will provide a useful new probe of the molecular content of inner disk winds. To date, there is no evidence for absorption in the rotational lines (except for tentative evidence in VW Cha, see Figure 8 in Banzatti et al. 2023a), which could therefore be unaffected.

Opacity and non-LTE effects—There are specific lines that should be handled carefully depending on the analysis and modeling tools that are going to be used. As shown above in Section 3.1.3, there is a large number of ortho-para pairs of lines that overlap in wavelength, and where line opacity overlap is necessary to correctly model their combined flux. Not all modeling tools include line opacity overlap, including some of the thermochemical codes that are being used for the analysis of infrared spectra from disks, so these lines should in case be excluded from the modeling.

Another important case that we have illustrated in this work is the presence of several $v = 1 - 1$ lines intermixed with $v = 0 - 0$ lines (Section 3.1.4). These should generally be populated in non-LTE conditions and will bias the results from model fits that assume LTE, either from simple slab models or more sophisticated disk models. These lines should either be ignored when fitting spectra with LTE models, or accounted for by implementing non-LTE excitation. The measured flux in these lines could be used to characterize the density of the emitting gas in the inner hot region where they are excited (Meijerink et al. 2009), expanding what ground-based spectra have initially provided (Section 5.1.2 in Banzatti et al. 2023a).

7.2.2. Step 2 - Water line-ratio diagnostic diagrams

After the water spectrum has been inspected and any contaminated lines removed, the line list provided with this work can be used to measure line properties for a series of general analysis steps. The fundamental lines listed in Table 1 can be directly used to obtain the line flux ratios and place any target on Figures 9 and 10 for general identification of its water temperature components and their distribution. Figure 22 visualizes the three principal directions to interpret an object position on the diagram in terms of the increasing emitting areas

of a 400 K and 170 K water components, and the column density of the 400 K component. Objects that exceed the model series to the right of the diagram are increasingly dominated by a pure 400 K component, those that exceed the diagram at the top are more dominated by a colder component down to 170 K. We have not explored colder temperatures, as they need far-infrared spectra to be characterized.

7.2.3. Step 3 - Use line kinematic information, if available

While the water line-flux-ratio diagnostic diagram has broad applicability to any observed spectrum, in the limited cases where line widths are partially broadened by Keplerian rotation their kinematics can be used to better characterize the radial distribution of the different temperature components (Figures 20 and 21). Beyond the very simple Doppler mapping procedure presented above, which can be used for quick reference and comparison across objects, the advantage of using Doppler-broadened line widths will be in the simultaneous modeling of line excitation and broadening that can be done for specific cases in the future. These limited cases will also provide an important reference for comparison to the larger number of cases where lines are unresolved (or stellar mass or disk inclination may be unknown) and only the line fluxes can be used in modeling the spectra (e.g. Figure 21).

From what observed in this sample, the ro-vibrational lines at $< 9 \mu\text{m}$ are commonly Doppler-broadened due to their excitation in an innermost region within 0.1–0.2 au, as shown by fully spectrally resolved data from the ground (Banzatti et al. 2023a). In this case, future work should be able to use the observed flux and line broadening to study the density of a region near the inner disk wall, provided that non-LTE excitation is accounted for in the modeling.

8. SUMMARY AND CONCLUDING REMARKS

The study of water emission in protoplanetary disks is now reaching the end of its second decade, with a plethora of spectra obtained from ground and space observatories with a wide range of resolving powers (from 700 of Spitzer-IRS to 90,000 of VLT-CRIRES and IRTF-iSHELL). By combining water spectra from multiple surveys, Banzatti et al. (2023a) recently summarized a series of fundamental questions:

1. which inner disk region(s) do the infrared water lines trace, and are there multiple water reservoirs (with different temperature and density);
2. what is the water abundance in inner disks and what regulates it (chemistry vs dynamics);

3. what is the relative role of different excitation processes, and is water emission in LTE;
4. is water present in a molecular inner disk wind; and
5. how can we correctly interpret the complex water spectra observed across infrared wavelengths within a unified picture of inner disks?

After two years of JWST observations, steps forward have been made in some of these topics, especially the detection of multiple temperature components or a temperature gradient in water emission from inner disks (see Section 1). In this work, by analyzing MIRI-MRS high-quality spectra observed in 25 disks as part of the JDISC Survey we have contributed to the list above as follows:

1. Water in inner disks is generally distributed over a region with a radial temperature gradient that can be approximated with three temperature components (~ 850 K, ~ 400 K, ~ 170 K). These components trace different radial locations between the inner disk rim and the water snowline (as demonstrated from the line broadening), and different disks show very different situations, from having only a compact hot region (e.g. CI Tau) to having a 5–10 times more extended region reaching sublimation temperatures (e.g. GQ Lup). The column density of the ~ 400 K shows a range of a factor ~ 10 in this sample, also suggesting a broad diversity across different disks. With only a handful of water lines with $E_u \sim 1000$ –1500 K detected by MIRI, water emission from temperatures down to ice sublimation is detected in some disks (Figure 10, and Muñoz-Romero et al. 2024a) but a detailed characterization of the water abundance across the snowline in disks will necessitate a high-resolution far-infrared observatory.
2. The line flux ratios of low (1500 K) and intermediate (3600 K) energy levels in comparison to the high levels (6000 K) anti-correlate with the ALMA dust disk radius in a selected sample of disks, consistent with the role of pebble drift in regulating the water abundance within snowline proposed before (Ciesla & Cuzzi 2006b; Banzatti et al. 2023b). However, the broader sample in this work, which includes multiple-star systems, inner dust cavities, and slightly younger embedded objects, shows a larger spread likely due to other effects related to age, dust depletion, and stellar multiplicity that should be investigated in future work.

3. Extending what found from ground-based surveys, the excitation of the entire ro-vibrational band at 5–8 μm is in non-LTE and the broader line widths in this band suggest a smaller emitting radius than the rotational band. Rotational lines in the first vibrational level ($v = 1 - 1$) also show evidence for non-LTE excitation, which should enable obtaining useful estimates of the molecular gas density.
4. Water may indeed be present in inner disk winds, as shown for the first time by detecting blue-shifted absorption in the high-inclination disk of IQ Tau. Going forward, under specific geometric conditions MIRI spectra may provide a new probe of the physical and chemical composition of inner

disk winds close to their launching radii at the disk surface.

5. In this work, we have identified a number of guidelines to identify and account for different excitation and broadening effects in MIRI spectra, which should be beneficial to the community for producing reliable analyses and consistent comparisons across large datasets in the future.

Facilities: JWST

Software: Matplotlib (Hunter 2007), NumPy (van der Walt et al. 2011), SciPy (Virtanen et al. 2020), Seaborn (Waskom 2021), Astropy (Astropy Collaboration et al. 2013, 2018, 2022), LMFIT (Newville et al. 2014), iSLAT (Johnson et al. 2024), spectools.ir (Salyk 2022)

APPENDIX

A. SAMPLE PROPERTIES AND MEASUREMENTS

Tables 2 and 3 report the sample properties and some fundamental measurements extracted in this work.

B. CONTINUUM SUBTRACTION

The continuum-subtraction algorithm presented in Pontoppidan et al. (2024)⁴ is a very effective empirical procedure designed to remove broad dust features under narrow gas line emission. As noted in the original paper, the procedure may subtract a small fraction of the gas emission in some regions of dense clustering of lines. For this reason, in applying the method to this sample we excluded the following regions: 6.4–6.91 μm for the most densely clustered part of the ro-vibrational water bands, 7.45–7.515 μm in case of strong HI emission (which sits on a cluster of water lines, see Figure 1), 13.4–14.1 μm for the broad Q-branches of HCN and C₂H₂, and 14.9–15 μm for the Q-branch of CO₂ when stronger than the nearby water emission. We also exclude the region at $> 28 \mu\text{m}$ where the MRS sensitivity drops (Pontoppidan et al. 2024). A modification we make to the algorithm is to apply different smoothing pixel windows and number of iterations at short versus long wavelengths, with a separation at 8–10 μm ; this is found necessary in most spectra in this sample to account for the different clustering of lines, the different spectral resolution, and the different dust features in the two wavelength ranges, with the long wavelengths often including more dust fea-

tures (see e.g. the case of GK Tau shown in Banzatti et al. 2023b).

Additionally, we use 200 line-free regions identified from the slab models in Figures 1 to 4 to apply a final small wavelength-dependent offset informed on where the flux is expected to be dominated by dust continuum. We find that this final step helps in getting closer to the underlying continuum especially at $< 8 \mu\text{m}$, where the clustered ro-vibrational bands of CO and water produce a pseudo-continuum, and at $> 20 \mu\text{m}$, where fringe residuals would otherwise be interpreted as emission lines in the original code, pushing the continuum too low. This final offset turns out to also be important when molecular absorption is present, since the procedure from Pontoppidan et al. (2024) is built on the assumption that any gas feature in the spectrum is in emission (i.e. the algorithm assumes the continuum to be at the bottom of the spectrum, not at the top). Absorption spectra from a molecular inner disk wind (like the one identified in IQ Tau in Figure 18) or a stellar photosphere would instead have the continuum in between or at the top of any gas features, and the line-free regions help in identifying where the actual continuum is. An example of this procedure as applied to CI Tau is shown in Figure 23.

C. UPDATES TO THE MIRI RESOLVING POWER

Table 4 reports updated fits to measured line FWHM to characterize the MIRI resolving power as presented

⁴ The code is available at <https://github.com/pontoppi/ctool>.

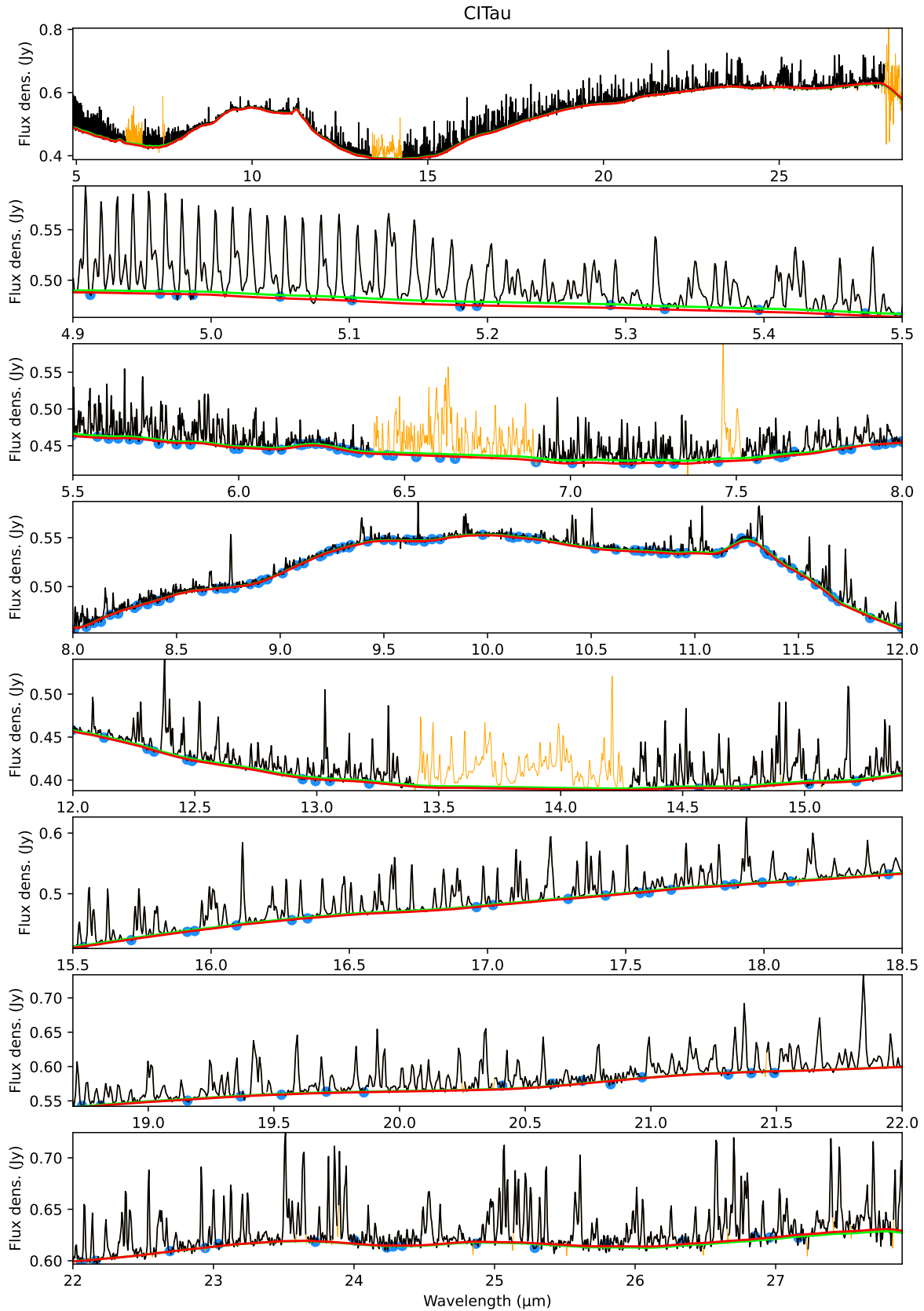


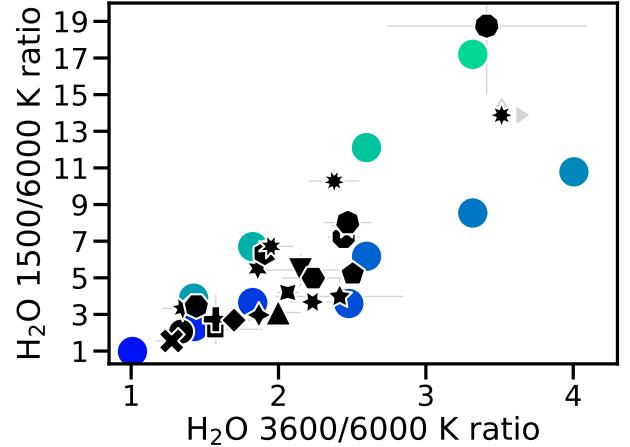
Figure 23. Example of the continuum subtraction procedure as applied to CI Tau. The entire original spectrum is shown at the top in black, and divided into smaller portions in the other panels. The excluded regions listed in Section B are colored in orange. The continuum estimated with the procedure described in Pontoppidan et al. (2024) is shown in light green. The red line shows the continuum after applying a wavelength-dependent offset determined from the line-free regions marked with blue points (see Section B).

Table 2. Sample properties used in this work as taken from the literature.

Name	Dist. (pc)	M_* (M_\odot)	$\log L_{\text{acc}}$ (L_\odot)	Incl. (deg)	R_{disk} (au)	Notes
AS205N	127	0.87	-0.07	20.0	50	binary
AS209	121	0.96	-1.12	35.0	138	...
CITau	160	0.71	-0.87	50.0	191	...
DoAr25	139	0.62	-2.13	67.4	166	cloud
DoAr33	143	0.69	...	42.0	27	...
Elias20	138	0.48	-0.87	49.0	65	cloud
Elias24	143	0.78	0.9	29.0	135	cloud
Elias27	118	0.49	...	56.0	257	cloud
FZTau	129	0.51	-0.27	22.0	12	...
GKTau	129	0.67	-1.38	38.8	13	...
GOTau	139	0.35	-2.0	53.9	170	cloud
GQLup	151	0.78	-0.36	60.5	56	binary
HPTau	177	1.20	...	18.3	22	...
HTLup	154	1.27	-1.18	48.0	25	binary
IQTau	131	0.50	-1.4	62.1	110	...
IRAS-04385	160	0.50	...	75.0	22	high incl.
MYLup	157	1.23	-0.7	73.2	87	high incl.
RULup	158	0.55	-0.01	19.0	63	...
RYLup	158	1.27	-1.4	68.0	135	cavity
SR4	132	0.68	-0.12	22.0	31	cloud
Sz114	162	0.17	-2.2	21.0	60	cloud
Sz129	159	0.83	-1.4	34.0	76	cavity
TWCha	183	0.70	-1.54	31.0	53	cavity
VZCha	191	0.50	-0.33	16.0	39	...
WSB52	142	0.48	-0.7	54.0	32	cloud

NOTE—References – distances are from GAIA (Gaia Collaboration et al. 2016, 2022), stellar and accretion properties are from Simon et al. (2016); Fang et al. (2018); Andrews et al. (2018); McClure (2019); Alcalá et al. (2019); Gangi et al. (2022); Manara et al. (2023); R_{disk} (taken as the radius enclosing 90–95% of emission depending on what reported in the original work) and disk inclinations are from Long et al. (2018); Tazzari et al. (2018); MacGregor et al. (2017); Ansdell et al. (2018); Long et al. (2019); Huang et al. (2018); Kurtovic et al. (2018); Hendler et al. (2020); Ribas et al. (2020). Cloud contamination as a sign of a more embedded younger object is reported when moderate to severe, as identified in Andrews et al. (2018); Long et al. (2022).

in Section 5.1 and Figure 16. We only update the intercept in sub-bands at $> 10\mu\text{m}$, since the slope was already well characterized in Pontoppidan et al. (2024); the parameters for sub-bands not included in this table are unchanged and can be found in Table 3 in Pontoppidan et al. (2024).

**Figure 24.** Same as Figure 9, but showing the flux ratio between the 1500 K and 6000 K lines (from Table 1).

D. LINEAR REGRESSION PARAMETERS

Table 5 reports linear regression parameters for significant correlations detected in this work. The data to reproduce these correlations are in Appendix A.

E. LINE LIST USED FOR THE ANALYSIS IN THIS WORK

Tables 6 and 7 report the list of single un-blended water transitions defined in Section 3 and used for the analysis in this work. The line list has been added to the GitHub repository of iSLAT for convenience to users.

F. ADDITIONAL PLOTS FOR THE WHOLE SAMPLE

Figures 24, 25, and 26 report additional plots to complement those shown in the main text above.

G. REFERENCE SLAB MODELS FOR THE ATLAS AND THE WATER DIAGNOSTIC DIAGRAMS

Table 8 reports the reference models used for the general water atlas in Figures 1 to 4. Table 9 reports the reference models used in Figure 9 for the water line-ratio diagnostic diagrams.

H. COMPACT WATER SPECTRAL ATLAS FOR JDISCS TARGETS

Figures 27 to 29 show a compact version of a water spectral atlas for all disks included in this work in reference to the three temperature components as in Figure 7. The spectra are split into three regions that are most important for the analysis presented in this work: the rotational lines at $\approx 15\text{--}18\mu\text{m}$ (typically dominated by water emission at higher temperatures), the rotational lines at $\approx 21\text{--}27\mu\text{m}$ (where cooler water emission,

Table 3. Sample measurements from this work.

Target	Ro-vib.	FWHM (km/s)				line flux (10^{-15} erg s $^{-1}$ cm $^{-2}$)					
		< 18 μ m	> 18 μ m	1500 K	3600 K	1500 K	3600 K	6000 K	3340 K (a)	3340 K (b)	
AS205N	110(9)	108(8)	137(8)	119(7)	104(5)	118(9)	140.79(10.44)	63.19(2.97)	28.26(2.34)	58.92(6.36)	42.33(1.61)
AS209	142(30)	148(28)	197(61)	...	149(18)	170(31)	11.20(5.35)	6.44(0.77)	4.09(0.41)	2.76(0.88)	(3.23)
CITau	138(14)	132(5)	160(15)	131(3)	135(4)	130(6)	10.06(0.35)	6.54(0.16)	4.89(0.23)	5.05(0.50)	5.58(0.16)
DoAr25	203(41)	155(13)	174(22)	123(11)	156(6)	157(9)	3.70(0.44)	2.39(0.10)	1.19(0.08)	2.80(0.18)	1.61(0.30)
DoAr33	155(28)	136(9)	155(12)	145(7)	135(6)	150(12)	2.61(0.17)	1.58(0.05)	0.71(0.05)	1.94(0.31)	1.23(0.10)
Elias20	126(42)	114(9)	138(7)	126(2)	111(4)	119(4)	45.83(0.75)	15.48(0.37)	6.34(0.23)	11.76(1.84)	13.63(0.37)
Elias24	117(18)	111(8)	140(5)	124(2)	112(4)	113(4)	104.82(1.66)	32.92(0.78)	13.37(0.45)	24.75(2.79)	31.39(0.45)
Elias27	116(7)	112(4)	141(6)	131(3)	110(4)	115(2)	21.92(0.67)	10.77(0.17)	5.22(0.17)	9.12(0.26)	7.99(0.51)
FZTau	100(4)	104(4)	135(9)	121(1)	107(4)	104(4)	43.34(0.71)	26.87(0.98)	14.43(0.73)	23.62(1.70)	20.60(0.75)
GKTau	128(12)	122(6)	161(23)	126(3)	122(4)	117(7)	22.27(0.63)	6.46(0.26)	3.32(0.22)	4.48(0.80)	6.72(0.20)
GOTau	115(39)	143(16)	169(36)	124(18)	143(9)	206(36)	0.81(0.16)	0.49(0.05)	0.20(0.03)	0.58(0.17)	0.40(0.12)
GQLup	116(30)	128(8)	151(25)	125(1)	128(5)	148(10)	30.79(0.47)	7.12(0.32)	3.00(0.17)	2.53(0.32)	8.60(0.45)
HPTau	119(11)	127(9)	148(33)	119(8)	138(10)	115(26)	10.97(0.97)	4.35(0.30)	2.03(0.29)	2.82(0.63)	4.14(0.36)
HTLup	176(27)	149(8)	166(44)	104(38)	150(9)	146(18)	8.81(4.83)	6.31(0.60)	4.02(0.73)	5.50(1.18)	2.71(1.47)
IQTau	94(31)	172(9)	180(35)	136(3)	179(8)	179(15)	9.85(0.25)	3.99(0.21)	2.95(0.26)	2.39(0.37)	3.03(0.05)
IRAS-04385	144(14)	122(13)	148(22)	118(4)	120(7)	126(20)	21.85(1.15)	3.98(0.15)	1.16(0.23)	4.11(0.93)	3.24(0.89)
MYLup	...	128(19)	152(45)	122(22)	152(32)	...	1.41(0.59)	0.23(0.06)	(0.05)	...	0.49(0.12)
RULup	99(8)	107(6)	140(17)	118(5)	107(3)	110(4)	37.78(2.21)	23.88(0.99)	14.06(0.72)	17.42(0.80)	15.96(1.72)
RYLup	120(39)	163(33)	136(28)	110(10)	177(50)	67(40)	5.37(0.61)	1.36(0.37)	0.39(0.29)	(0.26)	(0.27)
SR4	108(9)	124(5)	145(35)	112(9)	124(8)	132(13)	7.90(1.12)	6.49(0.45)	5.09(0.22)	3.59(0.59)	5.61(0.58)
Sz114	97(8)	102(7)	132(8)	117(5)	112(5)	97(5)	9.62(0.53)	2.96(0.06)	1.20(0.07)	2.08(0.38)	2.26(0.21)
Sz129	127(15)	119(6)	142(13)	127(4)	116(4)	123(4)	8.17(0.33)	2.46(0.06)	1.29(0.04)	1.04(0.10)	2.47(0.17)
TWCha	106(5)	107(4)	143(9)	127(2)	111(2)	109(2)	16.62(0.29)	5.61(0.10)	3.02(0.09)	2.45(0.11)	5.86(0.14)
VZCha	101(7)	107(4)	142(7)	126(1)	112(3)	109(3)	15.59(0.15)	6.50(0.21)	4.51(0.19)	4.03(0.61)	6.14(0.03)
WSB52	120(7)	115(7)	144(7)	127(3)	117(3)	117(3)	57.59(1.66)	27.69(0.37)	11.06(0.29)	30.58(1.06)	20.31(0.94)

NOTE—Lines are labelled according to their upper level energy as defined in Table 1. Uncertainties are shown in parentheses.

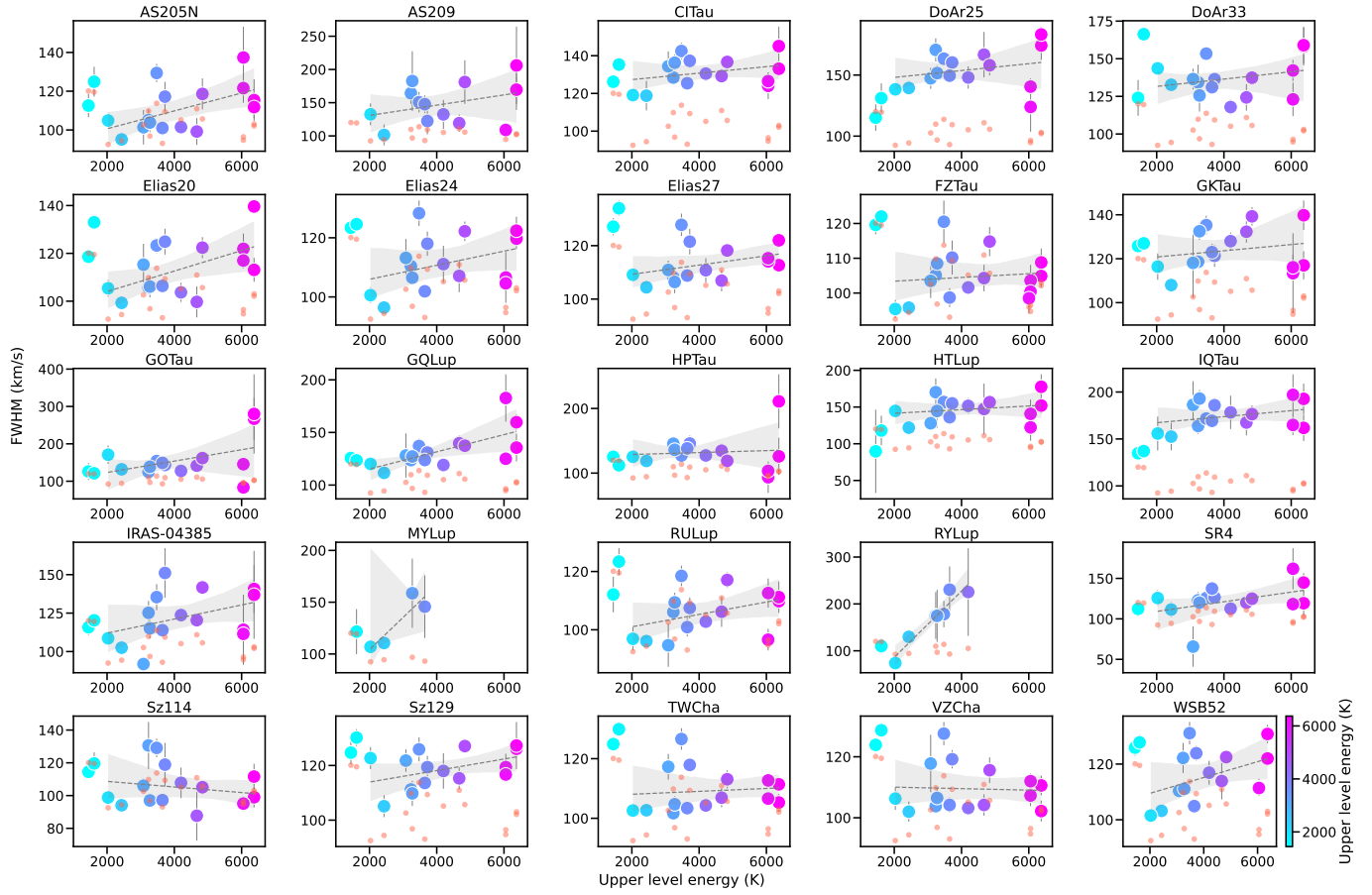


Figure 25. Same as Figure 17, but for the whole sample.

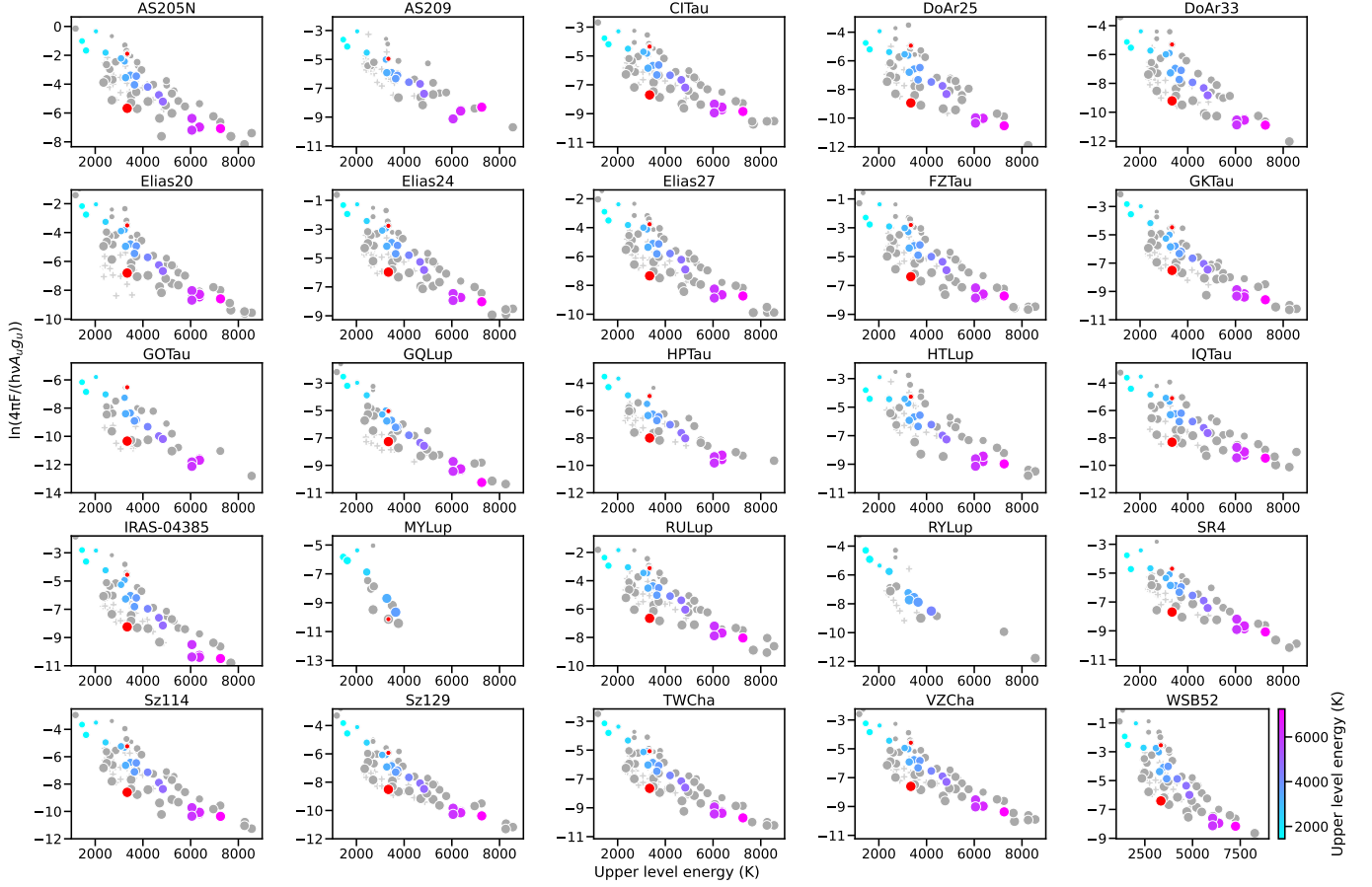


Figure 26. Rotation diagrams for the whole sample, following the same style as in Figure 8.

Table 4. MIRI resolving power.

Sub-band	a	b	Wavelength (μm)
1A	2742	150	5.66–6.63
2C	430	264	10.02–11.70
3C	-2240	312	15.41–17.98
4A	-2066	225	17.70–20.95
4B	-1076	150	20.69–24.48
4C	-3451	216	24.19–28.10

NOTE—Updates to Table 3 in Pontoppidan et al. (2024). The MIRI-MRS resolving power in each sub-band is reported as $\lambda/\Delta\lambda = R = a + b\lambda$.

where present, becomes prominent), and, lastly, the ro-vibrational band from the bending mode at 5–8 μm . The region of organic emission at 12–15.5 μm is included in the JDSCS overview paper (Arulanantham et al. 2024, in prep.). The line list presented in Section E is identified with stars, color-coded as in Figure 1. Targets in Figure 28 have some peculiarities: Sz 114 has the lowest stellar mass in this sample, IRAS 04385+2550 (labelled IRAS-04385 in the plots) is a younger more embedded disk, MY Lup has a very cold water spectrum analyzed in Salyk et al. (in prep.), HT Lup is the spectrum of both A and B components of the triple system, AS 209 and RY Lup have weaker molecular emission and larger fringe residuals than the rest of the sample.

REFERENCES

- Alcalá, J. M., Manara, C. F., France, K., et al. 2019, *A&A*, 629, A108
- Andrews, S. M., Huang, J., Pérez, L. M., et al. 2018, *ApJL*, 869, L41

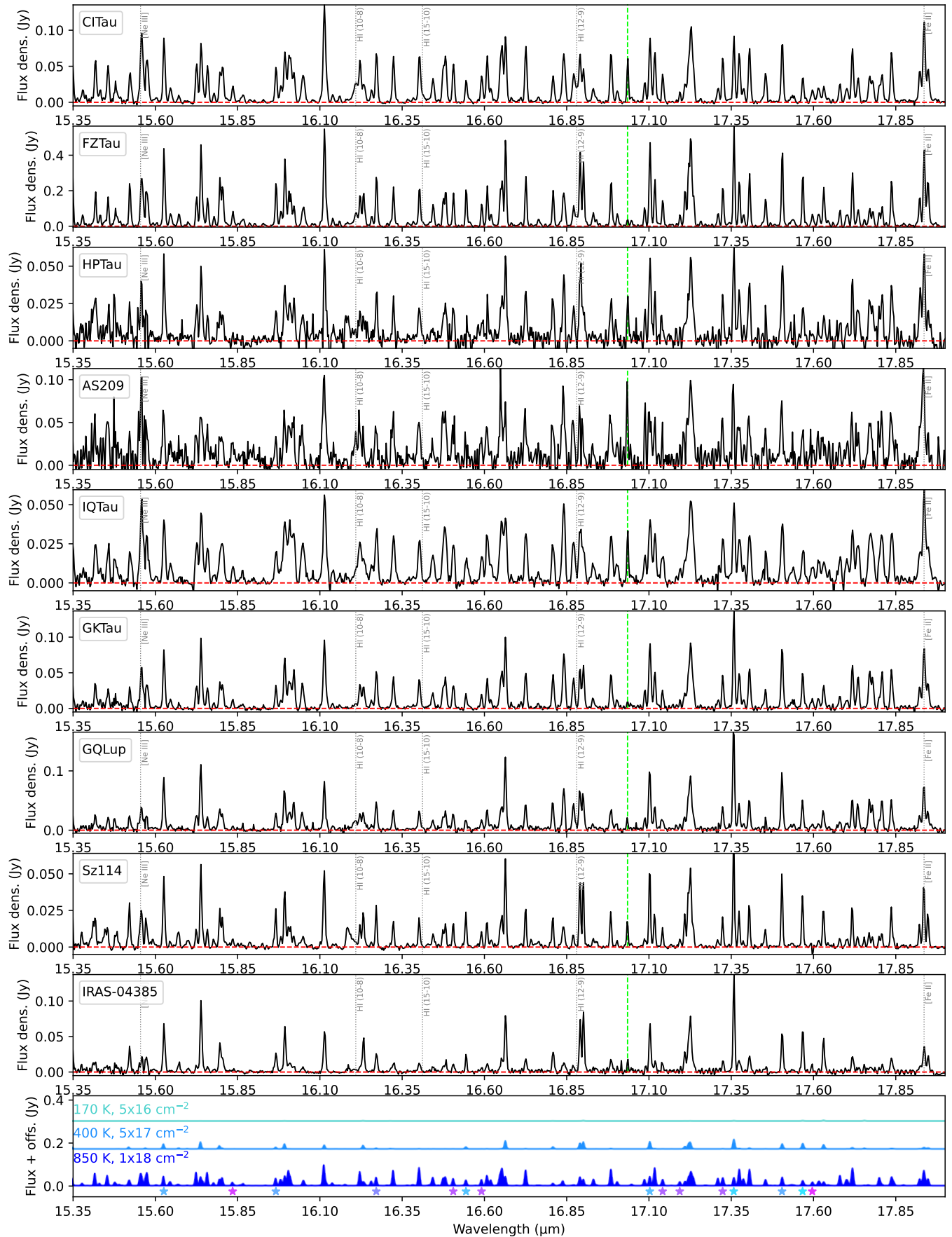


Figure 27. Compact water spectral atlas for JDISCS targets, highlighting the three temperature components discussed in the text. *NOTE: This figure will be expanded to include all other still unpublished spectra from this sample.*

Table 5. Linear regression parameters for correlations detected in this work.

x	y	$a(\sigma_a)$	$b(\sigma_b)$	Figure
$\log L_{1500K}$	$\log L_{acc}$	-4.58(0.12)	0.44(0.10)	11
$\log L_{3600K}$	$\log L_{acc}$	-4.92(0.11)	0.46(0.09)	11
$\log L_{6000K}$	$\log L_{acc}$	-5.19(0.11)	0.48(0.09)	11
$\log L_{3340K}$	$\log L_{acc}$	-5.02(0.13)	0.50(0.11)	11
$\log L_{1500K}$	Incl	-4.46(0.25)	-0.014(0.006)	11
$\log L_{3600K}$	Incl	-4.72(0.24)	-0.017(0.005)	11
$\log L_{6000K}$	Incl	-4.90(0.26)	-0.020(0.006)	11
$\log L_{3340K}$	Incl	-4.79(0.24)	-0.018(0.005)	11
1500/6000 K	$\log R_{disk}$	7.4(1.8)	-2.3(1.1)	13
3600/6000 K	$\log R_{disk}$	2.73(0.36)	-0.62(0.2)	13
FWHM(ro-vib.)	Incl	92(13)	0.72(0.31)	15
FWHM(rot<18 μ m)	Incl	96(8)	0.70(0.20)	15
FWHM(rot>18 μ m)	Incl	129(6)	0.52(0.14)	15
FWHM(OH 4000K)	Incl	109(21)	1.21(0.48)	15
FWHM(CO)	Incl	100(12)	0.76(0.27)	15
FWHM(rot<18 μ m)	FWHM(CO _{ground})	95(5)	0.44(0.07)	15
FWHM(rot>18 μ m)	FWHM(CO _{ground})	129(3)	0.32(0.04)	15
FWHM(OH 4000K)	FWHM(CO _{ground})	128(9)	0.33(0.13)	15

NOTE—Linear relations are in the form $y = a + bx$.

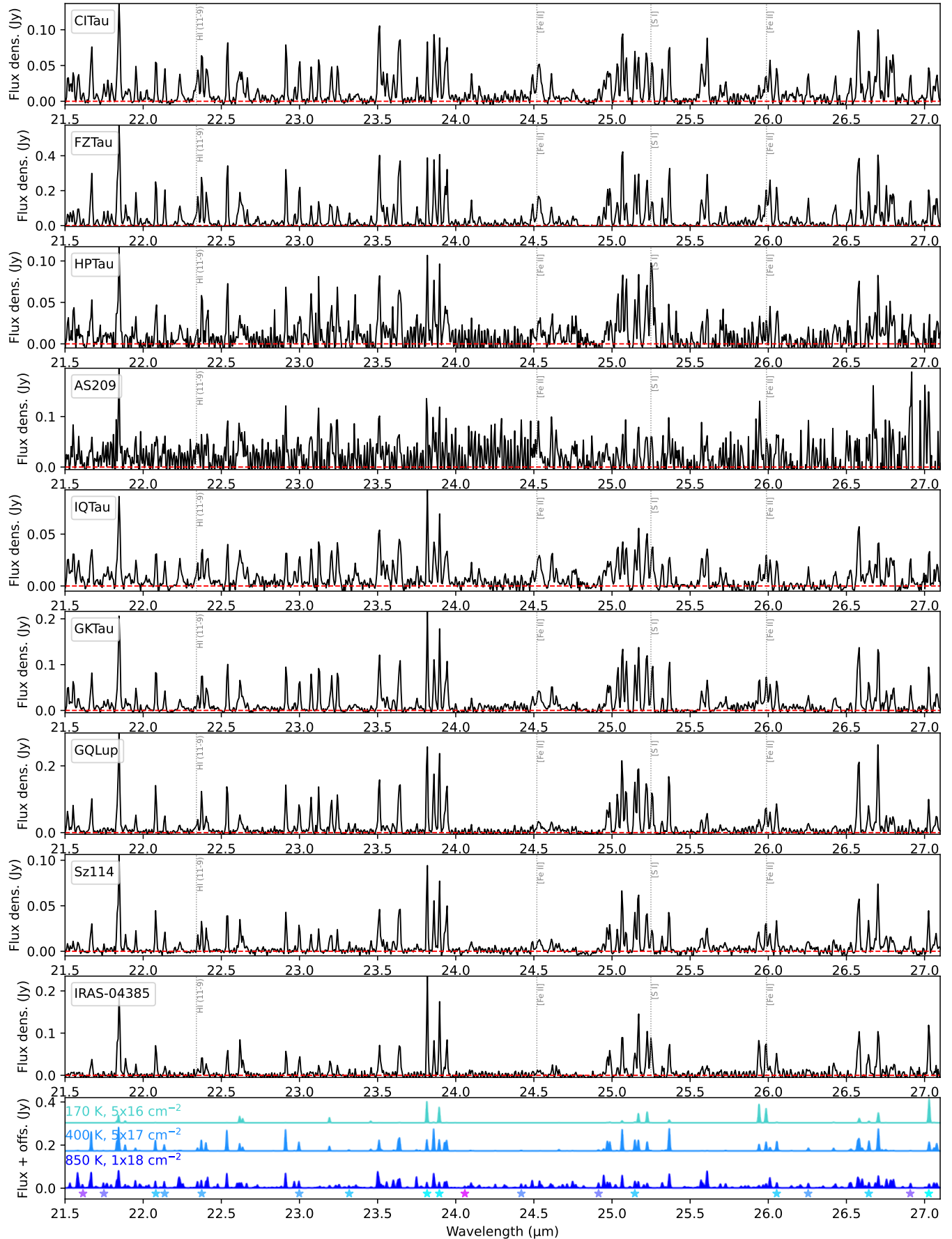


Figure 28. Same as Figure 27, but showing longer wavelengths. *NOTE: This figure will be expanded to include all other still unpublished spectra from this sample.*

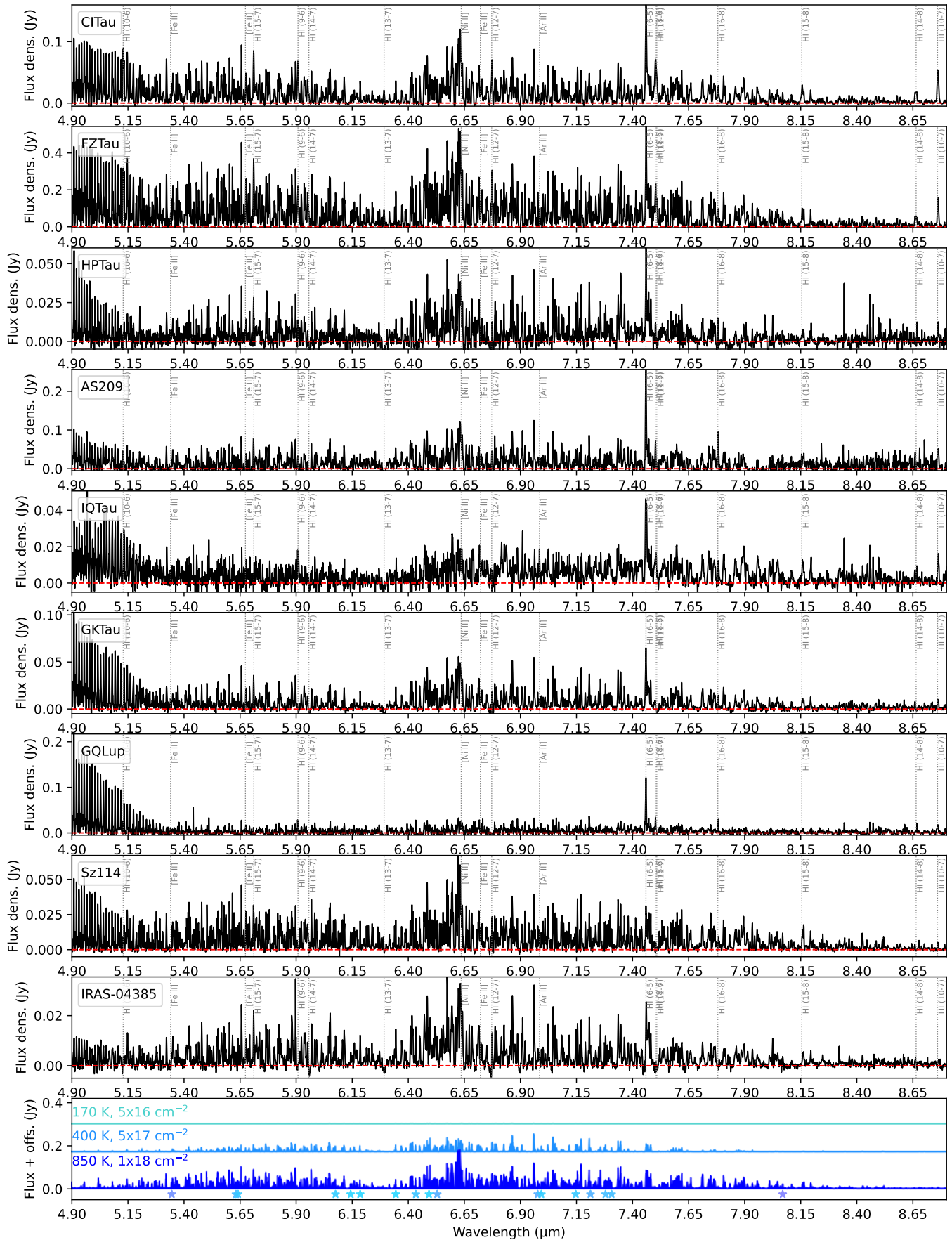


Figure 29. Same as Figure 27, but showing the ro-vibrational band. *NOTE: This figure will be expanded to include all other still unpublished spectra from this sample.*

Table 6. List of single un-blended water transitions defined in Section 3 and used for the analysis in this work.

Wavelength (μm)	Transitions (upper-lower) (level format: $v_1v_2v_3 J_{K_a K_c}$)	A_{ul} (s^{-1})	E_u (K)
5.34529	010-000 10 ₃₈ – 9 ₂₇	5.81	4420
5.63179	010-000 7 ₂₆ – 6 ₁₅	6.87	3335
5.64107	010-000 3 ₃₀ – 2 ₂₁	5.82	2744
5.80878	010-000 8 ₄₄ – 8 ₃₅	4.53	3987
6.07545	010-000 3 ₂₁ – 3 ₁₂	6.86	2617
6.14316	010-000 2 ₀₂ – 1 ₁₁	3.78	2395
6.1854	010-000 1 ₁₀ – 1 ₀₁	10.94	2360
6.34443	010-000 1 ₀₁ – 1 ₁₀	12.63	2328
6.43355	010-000 5 ₁₄ – 5 ₂₃	11.52	2878
6.49224	010-000 2 ₁₂ – 3 ₀₃	7.21	2412
6.52896	010-000 7 ₃₄ – 7 ₄₃	9.45	3543
6.97738	010-000 9 ₀₉ – 9 ₁₈	4.24	3614
6.99328	010-000 3 ₂₂ – 4 ₃₁	8.57	2609
7.14692	010-000 4 ₂₃ – 5 ₃₂	5.63	2745
7.21253	010-000 7 ₂₅ – 8 ₃₆	4.48	3442
7.27924	010-000 5 ₃₂ – 6 ₄₃	8.01	3065
7.30659	010-000 5 ₃₃ – 6 ₄₂	7.83	3059
8.0696	010-000 10 ₅₆ – 11 ₆₅	5.95	4867
9.90602	000-000 21 ₄₁₇ – 20 ₃₁₈	10.81	8270
10.1132	000-000 17 ₇₁₀ – 16 ₄₁₃	1.56	6371
10.76435	000-000 14 ₉₆ – 13 ₆₇	0.76	5302
10.85307	000-000 15 ₆₉ – 14 ₃₁₂	0.66	4996
11.00168	000-000 12 ₆₇ – 11 ₁₁₀	0.07	3501
11.17771	000-000 20 ₈₁₃ – 19 ₅₁₄	14.51	8556
11.26877	000-000 20 ₇₁₄ – 19 ₄₁₅	16.82	8257
11.64764	000-000 17 ₃₁₄ – 16 ₂₁₅	4.61	5483
11.70161	000-000 13 ₅₈ – 12 ₂₁₁	0.20	3783
11.96812	000-000 14 ₈₇ – 13 ₅₈	1.27	4985
12.26544	000-000 18 ₇₁₂ – 17 ₄₁₃	12.28	6953
12.5645	000-000 10 ₆₅ – 9 ₁₈	0.04	2697
12.89409	000-000 12 ₅₇ – 11 ₂₁₀	0.26	3310
12.98575	000-000 12 ₇₅ – 11 ₄₈	0.74	3759
13.13243	000-000 16 ₇₁₀ – 15 ₄₁₁	7.03	5763
13.29319	000-000 15 ₃₁₂ – 14 ₂₁₃	3.78	4431
13.31231	000-000 16 ₄₁₂ – 15 ₃₁₃	6.83	5213
13.50312	000-000 11 ₇₄ – 10 ₄₇	0.49	3340
14.34608	000-000 14 ₃₁₁ – 13 ₂₁₂	3.38	3941

NOTE—Line properties are from HITRAN (Gordon et al. 2022).

Table 7. List of single un-blended water transitions defined in Section 3 and used for the analysis in this work (continued).

Wavelength (μm)	Transitions (upper-lower) (level format: $v_1v_2v_3 J_{K_a K_c}$)	A_{ul} (s^{-1})	E_u (K)
14.42757	000-000 15 ₄₁₁ – 14 ₃₁₂	6.09	4668
14.51301	000-000 13 ₂₁₁ – 12 ₁₁₂	1.23	3232
14.89513	000-000 14 ₅₁₀ – 13 ₂₁₁	5.49	4198
15.62568	000-000 13 ₃₁₀ – 12 ₂₁₁	2.99	3474
15.83495	000-000 18 ₈₁₀ – 17 ₇₁₁	43.99	7252
15.96622	000-000 13 ₅₉ – 12 ₂₁₀	4.68	3721
16.27136	000-000 15 ₅₁₀ – 14 ₄₁₁	9.23	4835
16.50525	000-000 17 ₇₁₀ – 16 ₆₁₁	28.79	6371
16.54402	000-000 11 ₆₆ – 10 ₃₇	1.37	3082
16.59123	000-000 16 ₉₇ – 15 ₈₈	56.44	6369
17.10254	000-000 12 ₅₈ – 11 ₂₉	3.78	3273
17.14148	000-000 16 ₈₈ – 15 ₇₉	42.49	6053
17.19352	010-010 13 ₄₉ – 12 ₃₁₀	6.27	6005
17.32395	000-000 16 ₈₉ – 15 ₇₈	41.53	6051
17.35766	000-000 11 ₂₉ – 10 ₁₁₀	0.96	2432
17.50436	000-000 13 ₄₉ – 12 ₃₁₀	4.94	3645
17.56683	000-000 8 ₆₃ – 7 ₃₄	0.15	2030
17.59626	010-010 15 ₇₈ – 14 ₆₉	35.12	7686
18.25429	000-000 11 ₅₇ – 10 ₂₈	2.81	2857
19.12996	000-000 15 ₇₉ – 14 ₆₈	27.00	5214
19.24597	000-000 11 ₃₈ – 10 ₂₉	2.27	2608
19.34995	000-000 10 ₅₆ – 9 ₂₇	1.83	2472
19.68805	000-000 14 ₇₈ – 13 ₆₇	27.30	4696
20.42595	000-000 13 ₇₇ – 12 ₆₆	27.03	4211
20.66181	000-000 7 ₄₃ – 6 ₁₆	0.07	1339
21.33317	000-000 12 ₇₆ – 11 ₆₅	26.27	3759
21.61495	000-000 17 ₆₁₂ – 16 ₅₁₁	16.87	6073
21.7488	000-000 15 ₆₁₀ – 14 ₅₉	15.59	4953
22.08091	000-000 11 ₄₇ – 10 ₃₈	4.58	2732
22.13775	000-000 12 ₆₆ – 11 ₅₇	17.69	3507
22.37473	000-000 11 ₇₄ – 10 ₆₅	25.29	3340
22.99881	000-000 12 ₆₇ – 11 ₅₆	16.51	3501
23.31846	000-000 10 ₆₅ – 10 ₃₈	0.09	2697
23.81676	000-000 8 ₃₆ – 7 ₀₇	0.61	1447
23.89518	000-000 8 ₄₅ – 7 ₁₆	1.04	1615
24.05845	010-010 16 ₅₁₂ – 15 ₄₁₁	13.76	7640
24.41975	010-010 9 ₃₆ – 8 ₂₇	2.42	4179
24.91403	010-010 9 ₆₃ – 8 ₅₄	18.64	4778
25.14613	000-000 10 ₆₅ – 9 ₅₄	16.05	2697
26.05384	000-000 10 ₅₅ – 9 ₄₆	9.89	2481
26.25519	000-000 13 ₅₉ – 12 ₄₈	9.33	3721
26.64294	000-000 9 ₆₄ – 8 ₅₃	15.33	2346
26.90847	000-000 17 ₃₁₄ – 16 ₄₁₃	15.93	5483
27.0272	000-000 7 ₃₅ – 6 ₀₆	0.48	1175

NOTE—Line properties are from HITRAN (Gordon et al. 2022).

Table 8. Slab model parameters adopted in the water atlas (Figures 1 to 4).

Species	T (K)	N (cm^{-2})	R_{slab} (au)	A_{slab} (au^2)
H ₂ O hot (ro-vibr.)	850	1×10^{18}	0.25	0.2
H ₂ O hot	850	1×10^{18}	0.5	0.8
H ₂ O warm	400	5×10^{17}	0.9	2.5
H ₂ O cold	170	5×10^{16}	4	50
CO ₂	300	1×10^{17}	0.45	0.6
C ₂ H ₂	800	1×10^{16}	0.32	0.32
HCN	950	1×10^{16}	0.55	0.95
CO	1400	1×10^{18}	0.25	0.2
H ₂	400	1×10^{23}	4	50
OH hot	7000	1×10^{16}	0.1	0.03
OH warm	1000	1×10^{16}	0.7	1.5

NOTE—Other parameters that are assumed in the models: a distance of 160 pc, a thermal line broadening of 1 km/s (FWHM), an instrumental+Doppler line broadening of 130 km/s at $< 18\mu\text{m}$ and 160 km/s at longer wavelengths (as measured in CI Tau, see Section A). The only exception is H₂, which is distinctly narrower and is simulated with 95 km/s.

- Ansdell, M., Williams, J. P., Trapman, L., et al. 2018, *ApJ*, 859, 21
 Argyriou, I., Glasse, A., Law, D. R., et al. 2023, *A&A*, 675, A111
 Arulanantham, N., McClure, M. K., Pontoppidan, K., et al. 2024, *ApJL*, 965, L13
 Astropy Collaboration, Robitaille, T. P., Tollerud, E. J., et al. 2013, *A&A*, 558, A33
 Astropy Collaboration, Price-Whelan, A. M., Sipőcz, B. M., et al. 2018, *AJ*, 156, 123
 Astropy Collaboration, Price-Whelan, A. M., Lim, P. L., et al. 2022, *ApJ*, 935, 167
 Banzatti, A., Pontoppidan, K. M., Salyk, C., et al. 2017, *ApJ*, 834, 152
 Banzatti, A., Meyer, M. R., Bruderer, S., et al. 2012, *ApJ*, 745, 90
 Banzatti, A., Pascucci, I., Bosman, A. D., et al. 2020, *ApJ*, 903, 124
 Banzatti, A., Abernathy, K. M., Brittain, S., et al. 2022, *AJ*, 163, 174
 Banzatti, A., Pontoppidan, K. M., P ere Ch avez, J., et al. 2023a, *AJ*, 165, 72
 Banzatti, A., Pontoppidan, K. M., Carr, J. S., et al. 2023b, *ApJL*, 957, L22
 Bitsch, B., Raymond, S. N., & Izidoro, A. 2019, *A&A*, 624, A109
 Blevins, S. M., Pontoppidan, K. M., Banzatti, A., et al. 2016, *ApJ*, 818, 22
 Bosman, A. D., Bergin, E. A., Calahan, J., & Duval, S. E. 2022, *ApJL*, 930, L26
 Brown, J. M., Pontoppidan, K. M., van Dishoeck, E. F., et al. 2013, *ApJ*, 770, 94
 Bushouse, H., Eisenhamer, J., Dencheva, N., et al. 2024, JWST Calibration Pipeline, v1.15.1, Zenodo, doi:10.5281/zenodo.12692459, <https://doi.org/10.5281/zenodo.12692459>
 Carr, J. S., & Najita, J. R. 2008, *Science*, 319, 1504
 —. 2011, *ApJ*, 733, 102
 —. 2014, *ApJ*, 788, 66
 Ciesla, F. J., & Cuzzi, J. N. 2006a, *Icarus*, 181, 178
 —. 2006b, *Icarus*, 181, 178
 Delabrosse, V., Dougados, C., Cabrit, S., et al. 2024, arXiv e-prints, arXiv:2403.19400
 Drazkowska, J., Stammler, S. M., & Birnstiel, T. 2021, *A&A*, 647, A15
 Fang, M., Pascucci, I., Edwards, S., et al. 2018, *ApJ*, 868, 28
 Gaia Collaboration, Prusti, T., de Bruijne, J. H. J., et al. 2016, *A&A*, 595, A1
 Gaia Collaboration, Vallenari, A., Brown, A. G. A., et al. 2022, arXiv e-prints, arXiv:2208.00211
 Gangi, M., Antonucci, S., Biazzo, K., et al. 2022, *A&A*, 667, A124
 Gardner, J. P., Mather, J. C., Abbott, R., et al. 2023, *PASP*, 135, 068001
 Gasman, D., van Dishoeck, E. F., Grant, S. L., et al. 2023, *A&A*, 679, A117
 Glassgold, A. E., Meijerink, R., & Najita, J. R. 2009, *ApJ*, 701, 142
 Gordon, I. E., Rothman, L. S., Hargreaves, R. J., et al. 2022, *JQSRT*, 277, 107949
 Grant, S. L., van Dishoeck, E. F., Tabone, B., et al. 2023, *ApJL*, 947, L6
 Grant, S. L., Kurtovic, N. T., van Dishoeck, E. F., et al. 2024, arXiv e-prints, arXiv:2406.10217
 Hendler, N., Pascucci, I., Pinilla, P., et al. 2020, *ApJ*, 895, 126
 Henning, T., Kamp, I., Samland, M., et al. 2024, *PASP*, 136, 054302
 Houck, J. R., Roellig, T. L., van Cleve, J., et al. 2004, *ApJS*, 154, 18
 Huang, J., Andrews, S. M., Dullemond, C. P., et al. 2018, *ApJL*, 869, L42

Table 9. Series of slab models used in Figure 9.

Model	T (K)	N (cm^{-2})	R_{slab} (au)	M_{gas} (μM_{\oplus})	Combined models	1500/3600 K	3600/6000 K	1500/6000 K	3400 K b/a
H	850	1×10^{18}	0.5	0.9	H	0.97	1.01	0.97	0.79
W1	400	5×10^{17}	1.12	2.2	H+W1	1.64	1.43	2.34	1.39
W2	400	5×10^{17}	1.58	4.4	H+W2	2.00	1.83	3.65	1.84
W2(thick)	400	5×10^{18}	1.58	44	H+W2(Tk)	1.45	2.48	3.60	1.00
W3	400	5×10^{17}	2.24	8.9	H+W3	2.38	2.60	6.17	2.50
W4	400	5×10^{17}	2.74	13	H+W4	2.57	3.32	8.54	2.94
W5	400	5×10^{17}	3.16	18	H+W5	2.69	4.01	10.78	3.26
C1	170	5×10^{16}	8	11	H+W1+C1	2.73	1.42	3.89	1.39
C2	170	5×10^{16}	11.3	22	H+W2+C2	3.67	1.83	6.70	1.85
C3	170	5×10^{16}	16	45	H+W3+C3	4.66	2.60	12.11	2.50
C4	170	5×10^{16}	19.6	68	H+W4+C4	5.18	3.32	17.20	2.94
C5	170	5×10^{16}	22.6	90	H+W5+C5	5.50	4.00	21.97	3.26

NOTE—Other parameters that are assumed in the models: a distance of 160 pc, a thermal line broadening of 1 km/s (FWHM), an instrumental+Doppler line broadening of 130 km/s. M_{gas} is the observable gas mass (the product of area, column density, and molecular weight) in units of micro-Earth masses.

- Hunter, J. D. 2007, *Computing in Science and Engineering*, 9, 90
- Izidoro, A., Bitsch, B., Raymond, S. N., et al. 2021, *A&A*, 650, A152
- Jellison, E., Johnson, M., Banzatti, A., & Bruderer, S. 2024, arXiv e-prints, arXiv:2402.04060
- Johnson, M., Banzatti, A., Fuller, J., & Jellison, E. 2024, *spexod/iSLAT: Second release, vv4.03*, Zenodo, doi:10.5281/zenodo.12167853. <https://doi.org/10.5281/zenodo.12167853>
- Kalyaan, A., Pinilla, P., Krijt, S., Mulders, G. D., & Banzatti, A. 2021, *ApJ*, 921, 84
- Kalyaan, A., Pinilla, P., Krijt, S., et al. 2023, arXiv e-prints, arXiv:2307.01789
- Kamp, I., Honda, M., Nomura, H., et al. 2021, *PASA*, 38, e055
- Kamp, I., Henning, T., Arabhavi, A. M., et al. 2023, *Faraday Discussions*, 245, 112
- Krijt, S., Kama, M., McClure, M., et al. 2022, arXiv e-prints, arXiv:2203.10056
- Kurtovic, N. T., Pérez, L. M., Benisty, M., et al. 2018, *ApJL*, 869, L44
- Lambrechts, M., Morbidelli, A., Jacobson, S. A., et al. 2019, *A&A*, 627, A83
- Li, J., Boogert, A., & Tielens, A. G. G. M. 2024, *ApJS*, 273, 32
- Liu, Y., Pascucci, I., & Henning, T. 2019, *A&A*, 623, A106
- Lodders, K. 2003, *ApJ*, 591, 1220
- Long, F., Pinilla, P., Herczeg, G. J., et al. 2018, *ApJ*, 869, 17
- Long, F., Herczeg, G. J., Harsono, D., et al. 2019, *ApJ*, 882, 49
- Long, F., Andrews, S. M., Rosotti, G., et al. 2022, *ApJ*, 931, 6
- MacGregor, M. A., Wilner, D. J., Czekala, I., et al. 2017, *ApJ*, 835, 17
- Mah, J., Savvidou, S., & Bitsch, B. 2024, *A&A*, 686, L17
- Manara, C. F., Ansdell, M., Rosotti, G. P., et al. 2023, in *Astronomical Society of the Pacific Conference Series*, Vol. 534, *Protostars and Planets VII*, ed. S. Inutsuka, Y. Aikawa, T. Muto, K. Tomida, & M. Tamura, 539
- McClure, M. K. 2019, *A&A*, 632, A32
- Meijerink, R., Pontoppidan, K. M., Blake, G. A., Poelman, D. R., & Dullemond, C. P. 2009, *ApJ*, 704, 1471
- Muñoz-Romero, C. E., Banzatti, A., Öberg, K. I., et al. 2024a, arXiv e-prints, arXiv:2409.03831
- Muñoz-Romero, C. E., Öberg, K. I., Banzatti, A., et al. 2024b, *ApJ*, 964, 36
- Munoz-Romero, C. E., Banzatti, A., & Öberg, K. I. 2023, *iris (InfraRed Isothermal Slabs)*, Zenodo, doi:10.5281/zenodo.10369000
- Najita, J. R., Ádámkóvics, M., & Glassgold, A. E. 2011, *ApJ*, 743, 147
- Najita, J. R., Carr, J. S., Pontoppidan, K. M., et al. 2013, *ApJ*, 766, 134
- Najita, J. R., Carr, J. S., Salyk, C., et al. 2018, *ApJ*, 862, 122

- Newville, M., Stensitzki, T., Allen, D. B., & Ingargiola, A. 2014, LMFIT: Non-Linear Least-Square Minimization and Curve-Fitting for Python, v0.8.0, Zenodo, doi:10.5281/zenodo.11813
- Pascucci, I., Herczeg, G., Carr, J. S., & Bruderer, S. 2013, *ApJ*, 779, 178
- Perotti, G., Christiaens, V., Henning, T., et al. 2023, *Nature*, 620, 516
- Pollack, J. B., Hollenbach, D., Beckwith, S., et al. 1994, *ApJ*, 421, 615
- Pontoppidan, K., Battersby, C., Bergin, E., et al. 2023, in *American Astronomical Society Meeting Abstracts*, Vol. 241, American Astronomical Society Meeting Abstracts, 160.03
- Pontoppidan, K. M., Blake, G. A., & Smette, A. 2011, *ApJ*, 733, 84
- Pontoppidan, K. M., Salyk, C., Bergin, E. A., et al. 2014, in *Protostars and Planets VI*, ed. H. Beuther, R. S. Klessen, C. P. Dullemond, & T. Henning, 363
- Pontoppidan, K. M., Salyk, C., Blake, G. A., & Käuffl, H. U. 2010a, *ApJL*, 722, L173
- Pontoppidan, K. M., Salyk, C., Blake, G. A., et al. 2010b, *ApJ*, 720, 887
- Pontoppidan, K. M., Bergin, E. A., Melnick, G., et al. 2018, arXiv e-prints, arXiv:1804.00743
- Pontoppidan, K. M., Salyk, C., Banzatti, A., et al. 2024, *ApJ*, 963, 158
- Ramírez-Tannus, M. C., Bik, A., Cuijpers, L., et al. 2023, *ApJL*, 958, L30
- Ribas, Á., Espaillat, C. C., Macías, E., & Sarro, L. M. 2020, *A&A*, 642, A171
- Rieke, G. H., Wright, G. S., Böker, T., et al. 2015, *PASP*, 127, 584
- Rigliaco, E., Pascucci, I., Duchene, G., et al. 2015, *ApJ*, 801, 31
- Ros, K., & Johansen, A. 2013, *A&A*, 552, A137
- Salyk, C. 2022, csalyk/spectools.ir: First release, vv1.0.0, Zenodo, doi:10.5281/zenodo.5818682
- Salyk, C., Lacy, J., Richter, M., et al. 2019, *ApJ*, 874, 24
- Salyk, C., Pontoppidan, K. M., Blake, G. A., et al. 2008, *ApJL*, 676, L49
- Salyk, C., Pontoppidan, K. M., Blake, G. A., Najita, J. R., & Carr, J. S. 2011, *ApJ*, 731, 130
- Salyk, C., Yang, Y.-L., Pontoppidan, K. M., et al. 2024, arXiv e-prints, arXiv:2407.15303
- Sasselov, D. D., & Lecar, M. 2000, *ApJ*, 528, 995
- Schneider, A. D., & Bitsch, B. 2021, *A&A*, 654, A71
- Schwarz, K. R., Henning, T., Christiaens, V., et al. 2024, *ApJ*, 962, 8
- Simon, M. N., Pascucci, I., Edwards, S., et al. 2016, *ApJ*, 831, 169
- Tabone, B., van Dishoeck, E. F., & Black, J. H. 2024, arXiv e-prints, arXiv:2406.14560
- Tabone, B., van Hemert, M. C., van Dishoeck, E. F., & Black, J. H. 2021, *A&A*, 650, A192
- Tabone, B., Bettoni, G., van Dishoeck, E. F., et al. 2023, *Nature Astronomy*, 7, 805
- Tazzari, M., Beaujean, F., & Testi, L. 2018, *MNRAS*, 476, 4527
- Temmink, M., van Dishoeck, E. F., Gasman, D., et al. 2024, *A&A*, 689, A330
- van der Walt, S., Colbert, S. C., & Varoquaux, G. 2011, *Computing in Science and Engineering*, 13, 22
- van Dishoeck, E. F., Bergin, E. A., Lis, D. C., & Lunine, J. I. 2014, in *Protostars and Planets VI*, ed. H. Beuther, R. S. Klessen, C. P. Dullemond, & T. Henning, 835
- van Dishoeck, E. F., Grant, S., Tabone, B., et al. 2023, *Faraday Discussions*, 245, 52
- Virtanen, P., Gommers, R., Oliphant, T. E., et al. 2020, *Nature Methods*, 17, 261
- Waskom, M. 2021, *The Journal of Open Source Software*, 6, 3021
- Wells, M., Pel, J. W., Glasse, A., et al. 2015, *PASP*, 127, 646
- Wright, G. S., Rieke, G. H., Glasse, A., et al. 2023, *PASP*, 135, 048003
- Xie, C., Pascucci, I., Long, F., et al. 2023, *ApJL*, 959, L25
- Yang, Y.-L., Green, J. D., Pontoppidan, K. M., et al. 2022, arXiv e-prints, arXiv:2208.10673
- Zannese, M., Tabone, B., Habart, E., et al. 2024, *Nature Astronomy*, 8, 577
- Zhang, K., Pontoppidan, K. M., Salyk, C., & Blake, G. A. 2013, *ApJ*, 766, 82